ABSTRACT

Title of Dissertation: QUANTUM LIGHT GENERATION
FROM BOUND EXCITONS IN ZNSE

Aziz Karasahin
Doctor of Philosophy, 2022

Dissertation Directed by: Professor Edo Waks
Department of Electrical and Computer Engineering

Quantum light sources and spin based qubits are essential building blocks for on-chip scalable quantum computation and information processing. To achieve scalability, information-storing qubits should exhibit long coherence times. These qubits should also be efficiently interfaced with information-carrying single photons. Semiconductors are not only able to host such qubits and single photon sources but also they offer a platform to interface them with the help of photonic structures. Hence, optically active solid-state qubits such as quantum dots, crystal defects and color centers have been extensively studied to date in various semiconductors. However, we still lack of a suitable platform to satisfy all the requirements needed to realize a scalable quantum technology.

Impurities in epitaxially grown ZnSe are particularly promising single photon sources and qubit candidates due to the direct bandgap of the material and potential for isotopic purification to achieve nuclear spin-zero background. These impurities possess impurity-bound electrons that can serve as spin-qubit. They also form impurity-bound excitons

that can generate single photons. Various impurities have been studied in ZnSe, but only F impurities have been isolated as single emitters to date. Despite the great potential suggested by previous results, there are many impurities waiting to be explored for their quantum capabilities.

In this thesis, we study isolated Cl impurities in ZnSe for their photon emission and spin properties. We utilize a ZnMgSe/ZnSe/ZnMgSe quantum well to increase the binding energies bound excitons and to better separate donor bound exciton emission from the free excitons. In the PL spectrum, we observe narrow emission lines around 440 nm, which are originated from the single bound excitons. We calculate the average binding energy as 15 meV (at least 2 times higher than bulk values) and inhomogeneous broadening as 6 meV. We confirm the single photon emission by observing clear photon antibunching in the second order autocorrelation measurements. The time-resolved photoluminescence measurements show short radiative lifetimes of 192 ps. Our results demonstrate first time isolation of donor impurities in an unstructured ZnSe, and provides complete characterization of radiative properties single Cl bound excitons.

The bound electron of a donor impurity atom can serve as a spin qubit. We verify that the presence of ground state electron of the Cl donor complex by observing two-electron satellite emission. We also characterize the Zeeman splitting of the exciton transitions by performing polarization-resolved magnetic spectroscopy on the single emitters.

We also discover the presence of single biexcitons bound to Cl impurities. We demonstrate a radiative cascade from the decay of bound biexcitons. The emission exhibits both single photon statistics and clear temporal correlations revealing the time–ordering of the cascade.

Finally, we discuss the design of nanophotonic cavities in the ZnSe platform. We develop a nanofabrication recipe to create suspended photonic crystal cavities. Then, we optically characterize the fabricated cavities.

The results presented in this thesis provide the first complete study of single Cl impurities in ZnSe. Based on the results discussed, single Cl impurities in ZnSe manifest themselves as promising quantum light sources and appealing solid-state qubit candidates.

QUANTUM LIGHT GENERATION FROM BOUND EXCITONS IN ZNSE

by

Aziz Karasahin

Dissertation submitted to the Faculty of the Graduate School of the
University of Maryland, College Park in partial fulfillment
of the requirements for the degree of
Doctor of Philosophy
2022

Advisory Committee:
Professor Edo Waks, Chair & Advisor
Professor Cheng Gong
Professor Avik Dutt
Professor Rajarshi Roy
Professor Oded Rabin, Dean's Representative

Dedication

To my better half, my dear Hatice

Acknowledgments

All praise be to God, the Lord of worlds, for his countless graces and blessings, endowing me with faith, life, patience and the will to pursue the science in the name of him.

My most special thanks go to my beloved wife, Hatice, for her continued support at every moment, her patience in moments of struggle and her the most beautiful heart. She has always made me smile, even in the most difficult times. Her unconditional love has enlightened my days and nights, and made our home a lovely nest.

This thesis would not be possible without many supervisors, colleagues and peers. I would like express my gratitude to my advisor, Edo Waks, for giving me an invaluable opportunity to work on challenging projects in his group. His scientific approach and breadth of ideas have made this thesis possible. I am grateful to Dr. Robert M. Pettit who joined the group at times that I had been struggling with experiments. Thanks to his experience, endless patience and scientific curiosity, this study gave fruits.

I would like to thank Professor Avik Dutt, Professor Cheng Gong, Professor Rajarshi Roy and Professor Oded Rabin for agreeing to serve on my thesis committee and for sparing their invaluable time reviewing the manuscript. I would like to also thank Professor Mohammad Hafezi for serving in my proposal committee and our exciting collaboration in the first half of my PhD. He is one the best scientists that I have ever met.

All samples studied in this thesis are supplied by our colleagues, Professor Alexander Pawlis and his team at Jülich, Marvin Marco Jansen, Nils von den Driesch and Yurii Kotovyi. I thank them for the incredible collaboration.

My friends and peers at the Quantum Nanophotonics Group have enriched my graduate life in many ways and deserve a special mention. I would like to thank Sabyasachi Barik for answering my endless questions always with enthusiasm. I learnt many experimental skills and optical alignment tricks from him. He was not only incredible lab mate but also a good friend outside of the lab. I did not know that Zhouchen Luo would be the best office mate when I met him as first person in the campus. His dedication has always made me amazed. I had many valuable interactions with other group members, to name some, Subhojit Dutta, Mustafa Buyukkaya, Dr. Changmin Lee, Harjot Singh, Shahriar Aghahei, Dr. Je-Hyung Kim, Uday Saha, Dr. Dima Farfurnik, Yuqi Zhao, Sam Harper, Tao Cai, Shuo Sun and many others. They all made the IREAP home far away from my country. I will always remember my beautiful memories with them.

I am grateful for the support from the staff in the Maryland NanoCenter: Tom Loughran, Mark Lecates, Jon Hummel and John Abrahams, Jiancun Rao and Sz-Chian Liou. I especially thank Valery Ray for teaching me how to use SEM and FIB. He is not only a great expert but also a humble teacher. I would like to also thank all the staff members in IREAP, including Don Schmadel, Nolan Ballew and Bryan Quinn for their technical support that enabled complex experiments. I would like to thank IREAP administrative office staff, including Nancy Boone, Judi Cohn Gorski, Dorothea Brosius and Leslie Delabar for their great assistance with purchases, payrolls and all other administrative works.

I would like to acknowledge financial support from the Air Force Office of Scientific Research (AFOSR), Maryland- ARL Quantum Partnership, National Science Foundation (NSF), Physics Frontier Center (PFC) at the Joint Quantum Institute (JQI) and German Research Fund (DFG) for all the projects discussed herein.

Lastly, I would like to thank my mom, dad, sister for being there for these long years. I have been always fortunate to have parents that supported me since my childhood and respected my choices. I am grateful for my both grandmothers's prayers which gave me the power to finish this journey. I hope this thesis and my success will relieve their longing eyes.

Table of Contents

Dedication ii

Acknowledgements iii

Table of Contents vi

List of Figures viii

List of Abbreviations xi

Chapter 1: Introduction 1
- 1.1 Quantum Computing and Information Processing . . . 1
- 1.2 Some Concepts . . . 2
- 1.3 Motivation for This Study . . . 4
- 1.4 Thesis Outline . . . 6

Chapter 2: Bound Excitons in ZnSe 7
- 2.1 Crystal Structure . . . 8
- 2.2 Donor Bound Exciton State . . . 9

Chapter 3: Material Growth 12
- 3.1 MBE Growth . . . 12
  - 3.1.1 Delta Doping of Cl Impurities . . . 14
- 3.2 The Effect of Quantum Confinement . . . 14

Chapter 4: Radiative Properties of Single Bound Excitons 16
- 4.1 Introduction . . . 16
- 4.2 Photoluminescence Characterization . . . 17
  - 4.2.1 Measurement Details . . . 17
  - 4.2.2 Photoluminescence Spectrum . . . 18
  - 4.2.3 Binding Energies & Inhomogeneous Broadening . . . 23
  - 4.2.4 Stability . . . 25
- 4.3 PLE Measurements . . . 28
- 4.4 Lifetime of Emitters . . . 30
- 4.5 Single Photon Generation . . . 33
- 4.6 Temperature Tuning of the Emission . . . 37
- 4.7 Summary . . . 40

Chapter 5: Spin States of Bound Electrons 41
5.1 Two-Electron Satellite Emission . . . 42
5.2 Donor Electron Energy States under Magnetic Field . . . 45
5.2.1 Energy Splitting . . . 47
5.2.2 Optical Selection Rules . . . 48
5.3 Magnetospectroscopy Experiments . . . 50
5.3.1 Measurement Setup . . . 50
5.3.2 Faraday Magnetic Field . . . 51
5.3.3 Voigt Magnetic Field . . . 54
5.4 Summary . . . 54

Chapter 6: Cascaded Single Photon Emission from Biexcitons 55
6.1 Radiative Cascades from Biexcitonic Decay . . . 56
6.2 Experiment Setup . . . 57
6.3 Demonstration of Cascaded Single Photon Emission . . . 59
6.3.1 Characteristics of PL Response . . . 59
6.3.2 Time Resolved Spectroscopy Results . . . 61
6.3.3 Photon Correlation Measurements . . . 64
6.4 Fine Structure Splitting and Polarization Response . . . 67
6.5 Summary . . . 72

Chapter 7: Design and Fabrication of Nanophotonic Cavities 73
7.1 Introduction . . . 73
7.2 Design of L3 Photonic Crystal Cavities . . . 75
7.3 Fabrication of Cavities . . . 77
7.4 Optical Characterization . . . 81
7.5 Discussions . . . 83

Chapter 8: Conclusion and Outlook 85

Appendix A: Fabrication Details 89
A.1 Nanofabrication Recipe for ZnSe Photonic Crystals . . . 89

Appendix B: Other Research Contributions 93
B.1 Demonstration of Robust Quantum Photonic Devices with Topological Edge States . . . 93
B.2 Integration of Quantum Emitters with Telecom Photonics . . . 94

Appendix C: List of Publications and Conference Talks 97

Bibliography 99

Bibliography 99

List of Figures

2.1 Crystal structure of ZnSe with a single Cl impurity substituting a Se atom. 9
2.2 Energy band diagram showing the ground state (D^0) and excited state (D^0X), along with the bound exciton and two-electron-satellite emission, shown as blue and red arrow, respectively. 10

3.1 Layer structure of the grown material with in-situ doped Cl impurities in the ZnSe quantum well. 13

4.1 Photoluminescence response obtained with the above band excitation. a) Schematic illustrating the excitation and recombination mechanisms of the observed FX and D^0X lines. b) PL spectrum demonstrating free exciton (FX), trion (X^-) and bound exciton (D^0X) emission. 20
4.2 a) Power dependent intensity of bound exciton (blue) and free exciton (red), showing saturation of bound exciton lines. b) Power dependent intensity plotted in log scale for low powers up to 20 μW, showing linear dependence for both free exciton and bound exciton emission. 22
4.3 Linewidth of bound exciton line, extracted from Lorentzian curve fitting, showing a linear dependence on the excitation power. Extrapolation to zero power shows significant homogeneous broadening, that could be due to charge instabilities and temperature induced effects. 24
4.4 Histogram showing the distribution of binding energies of D^0X lines, with an average binding energy of 15 meV and a standard deviation of 6 meV. 26
4.5 PL intensity recorded over 7 hrs showing the stability of the emitter. . . . 27
4.6 Photoluminescence excitation a) Schematic illustration showing how resonant excitation of FX line creates bound excitons. b) PLE spectrum of bound exciton line obtained by tuning the pump laser over the FX line. 29
4.7 Time resolved lifetime measurement setup a) The measurement configuration to characterize the timing response of the measurement system. b) The instrument response function (IRF) showing the limited time resolution caused by detector timing jitter. 30
4.8 Time-resolved photoluminescence measurement, showing biexponential decay with dominant fast decay component of 192 ps and slow decay component of 2.49 ns. 32

4.9 The schematic of the setup to measure the autocorrelation function from the D^0X line. First, the collected light is filtered with the monochromator, then photons originated from bound exciton emission are sent to the identical detectors. We enclose the detectors to avoid the room light contribution. . 34
4.10 a) Coincidence counts of two detectors with variable time delay, obtained with 60 hours of integration, showing emitted photons are single. b) Noise corrected second-order auto-correlation function obtained from the single line, demonstrating almost perfect photon antibunching. 36
4.11 Temperature tuning of the emission. a) PL spectrum obtained at increasing sample temperatures up to 70K. b) The relative shift of emission energies of FX and D^0X lines from the 3.6K values, showing a similar temperature dependence for both curves. c) Temperature dependent linewidth showing that significant broadening starts at 60K 39

5.1 Spectrums showing the TES line with increasing resonant pump. power . 43
5.2 Background corrected and integrated counts from dashed spectral window showing saturation of TES line with increasing pump power. 44
5.3 Energy levels and spin configurations of the (ground) bound electron and (excited) bound exciton states. 46
5.4 Zeeman splittings of ground and excited states of bound exciton, along with optical transitions under Faraday magnetic field. 49
5.5 Zeeman splittings of ground and excited states of bound exciton, along with optical transitions under Voigt magnetic field. 50
5.6 Optical setup to measure PL under the applied magnetic field. a and b) Schematic demonstrating the configuration of the insert (composed of XYZ stage, the sample, and the collection lens) for Faraday (Voigt) field measurements. c) The picture of the Attocube sample insert. 52
5.7 Polarization resolved photoluminescence spectrum recorded at increasing magnetic field intensity, showing the splitting of orthogonal circular polarizations. 53

6.1 Schematic of the optical setup used to investigate optical properties of exciton-biexciton complexes. 58
6.2 Photoluminescence spectrum measured with above band continous wave laser excitation, showing free exciton (FX), bound exciton (D^*_AX, D^*_BX) and biexciton (D^*_AXX, D^*_BXX) states 60
6.3 a) Power dependent intensity for exciton and biexciton lines b) Energy levels showing exciton and biexciton states c) Time resolved PL intensity showing delayed emission from exciton lines in the presence of biexcitonic emission. 61
6.4 PL intensity recorded for 10 minutes showing spectral wandering and intensity correlations between exciton-biexciton lines, for A (top) and B lines (bottom). 63

6.5 Single photon correlation measurements. (a,b) Autocorrelation measurements of (a) the localized exciton line, $g^{(2)}_{X}(\tau)$, and (b) the localized biexciton line, $g^{(2)}_{XX}(\tau)$. (c,d) Cross–correlation measurements between the localized exciton and biexciton lines, $g^{(2)}_{X,XX}(\tau)$, with (c) pulsed excitation and (d) continuous wave excitation above the quantum well barrier. 65
6.6 Polarization resolved spectroscopy. (a) Measured polarized fine structure of the $D^{*}_{A}X$ and $D^{*}_{A}XX$ lines. (b) Polarization analysis of the $D^{*}_{A}X$ and $D^{*}_{A}XX$ fine structure as a funciton of quarter wave plate angle. 68

7.1 Schematic of L3 cavity. Three missing holes as linear line at the center, labeled as c, forms the cavity in the triangular lattice. The geometrical parameters optimized for the design has been labeled as lattice constant (L), radius (r), displacements (a,b,d). 75
7.2 FDTD simulation results. a) Electric field intensity distribution of the fundamental mode at the resonance b) Far field radiation pattern of high-Q design c) Far field radiation pattern of lower-Q design 77
7.3 Nanofabrication steps to create suspended photonic crystal cavities 78
7.4 SEM images of fabricated photonic crystal cavities. a) Cross sectional view of the etched lines, showing the directionality of the dry etch process. b) Top view showing the triangular lattice with 3 missing holes, forming L3 cavity. Inset shows the close up image of the cavity region. Rectangular holes around the structure are etched to facilitate undercutting of GaAs to make structures suspended. c) Angled view image of the fabricated device, showing that substrate is not etched completely. 80
7.5 Layer structure of the fabricated devices. Left image shows the the sample in-use. Lack of sacrificial layer resulted in non-selective etching of GaAs. Right image shows the proposed structure with AlGaAs sacrificial layer. . 82
7.6 The measured spectrum of the sample. Blue line shows PL spectrum from unpatterned bulk region. The orange curves demonstrates cavity mode with q-factor of 110. The low q-factor is caused by radiative losses, due to non-perfect undercutting. 84

List of Abbreviations

AlAs	Aluminum Arsenide
AlGaAs	Aluminum Gallium Arsenide
CCD	Charged Coupled Device
Cl	Chlorine
CW	Continous Wave
EBL	Electron Beam Lithography
F	Flourine
FDTD	Finite Difference Time Domain
FWHM	Full Width Half Maximum
FX	Free Exciton
GaAs	Gallium Arsenide
HH	Heavy-hole
ICP-RIE	Inductively Coupled Plasma-Reactive Ion Etching
InAs	Indium Arsenide
InP	Indium Phosphide
LL	Light-hole
MBE	Molecular Beam Epitaxy
NA	Numerical Aperture
PC	Photonic Crystal
PECVD	Plasma Enhanced Chemical Vapor Deposition
PIC	Photonic Integrated Circuit
PL	Photoluminescence
PLE	Photoluminescence Excitation
QD	Quantum Dot
QIP	Quantum Information Processing
QW	Quantum Well
Se	Selenium
TES	Two-Electron Satellite
ZnSe	Zinc Selenide
ZnMgSe	Zinc Magnesium Selenide
SiN	Silicon Nitride
SEM	Scanning Electron Microscope

Chapter 1: Introduction

1.1 Quantum Computing and Information Processing

In today's classical digital computers, the information is encoded as bits, 0 or 1, usually in the form of physical state of a classical system such as stationary charge or flowing electrical current. The information is processed by manipulation of the state by using logical gates. As we have witnessed miracles of the electronics technology in the last century, more challenging computational problems have emerged, sometimes practically impossible to solve with classical computers. Some of these hard problems can be addressed by recently developed algorithms based on a new type of computational approach, called quantum computing [1]. These algorithms are using advantage of the quantum states of the matter that are not available with classical systems to perform mathematical operations. In addition to enabling quantum computers, quantum mechanics can also be used for other applications such as secure communication (quantum key distribution) [2] and advanced sensing [3]. Hence, due to these great potential benefits, there is a growing interest in research community to engineer feasible quantum systems that can realize the proposed operations.

It is hard to predict the form of most suitable quantum hardware that will operate robustly in a practical setting. The qubits, quantum counterparts of classical bits, can be

constructed with various quantum systems such as spin states of electrons [4], superconducting circuits [5] or polarization of single photons [6]. Although the very basic units of quantum computation have been demonstrated with all these systems, there are still unsolved engineering issues to realize truly scalable system to perform complex tasks.

1.2 Some Concepts

Regardless of the form of the quantum device, the requirements to create robust devices to perform quantum operations can be generalized [7]. The performance of a quantum computer depends on the capability of satisfying all these requirements. However, often times, it is hard to find a system that can satisfy all requirements at once. Hence, the motivation of this research is to study a new platform to examine its capabilities for the quantum computing and quantum information applications.

Before discussing the content of my research, here, I would like to briefly introduce some concepts and requirements to the reader.

Stationary qubits are localized quantum states where the information can be written, read and stored. The quantum state is not often isolated from the environment. Hence, due to the interactions, fragile quantum information is lost over short a time duration, usually much less than seconds. For example, spin qubits can be formed by spin of a particle such as electron. When the qubit is in the superposition state of spin-up and spin-down, the relative phase and amplitude of superposition state will be preserved for certain amount of time until the system decays to more favorable energy state. The amount of time that qubit can store the information is called as decoherence time.

Three well known decoherence mechanisms are defined to quantify the total decoherence time [8]. T_1 is called the spin-lattice relaxation time, which represents the time it takes flipping of spin from one state to another, usually exchanging energy with phonons in the crystal. T_2 is called intrinsic decoherence time, which represents the time it takes loosing the phase information in the spin superposition state. T_2^* is called spin dephasing time, which represents the time it takes losing the coherence of spin vector. Usually, T_2 is the shortest among three and it sets the limit time duration a qubit can store information. Spin dephasing and coherence times are usually limited due to interactions between single spins and spin background of the host crystal. The broader goal is to find qubits or engineer materials such that long coherence times can be achieved. The decoherence times ranging from nanoseconds to seconds have been reported in the literature. The trapped ions usually are well isolated in the vacuum, hence they exhibit decoherence times longer than seconds [9]. The solid state systems such as impurities and defects in crystals usually exhibits much less decoherence times in the order of miliseconds to nanoseconds [10]. To date, spin coherence times of single donor impurities in ZnSe have not been reported yet, however, ensemble measurements showed coherence times that are in the order of nanoseconds [11].

To create interactions between different localized qubits, single quantum particles that have ability to transport the information (such as photons) should be used. Interfacing the stationary qubits with photons can allow mapping the qubit state to the photon state (such as polarization). This interfaces are called spin-photon interfaces. They form the fundamental pieces to realize quantum gates by allowing reading, writing and manipulating the spin state [12].

To realize efficient interactions between many spin qubits, single photons should exhibit number of features. First, photons emitted from different emitters should be indistinguishable in terms of wavelength and polarization. The figure of merit describing the ”indistinguishability” of photons are called homogeneity. Secondly, we should be able to create a large number of single photons to have multiple operations within the decoherence time of qubits. The ability to generate single photons in a given time interval is called brightness. The brightness of the emitter is limited by the radiative lifetime of the emitters. Hence, short radiative lifetimes usually result in more number of photons per second. (higher ”brightness”).

Interfacing stationary qubits and single photons is a challenging task due to the probabilistic nature of the interaction. To increase the efficiency of the process and to create more deterministic interactions, nanophotonic devices that enhance light-matter interactions are employed [13]. Due our capability to process semiconductors to create such interfaces, solid state qubits based on semiconductors usually offer more practical and scalable approach to realize scalable quantum computing.

1.3 Motivation for This Study

Impurities in wide-bandgap semiconductors are promising candidates to address all requirements and to create quantum photonic devices [14–16]. These isolated impurities generate single photons that exhibit transform-limited linewidths [17,18] and small inhomogeneous broadening [19,20] through their radiative optical transitions. Impurity atoms also provide isolated bound electrons [21] or holes [22] that can serve as spin-photon interfaces with

long coherence times [23, 24]. Furthermore, semiconductor fabrication and integration methods allow efficient spin-photon interfaces [25–27]. Hence, these platforms could satisfy major requirements of scalable quantum technology by combining pristine radiative properties with long-coherence time spin qubits in a practical setting.

Zinc Selenide (ZnSe) is appealing material as the host crystal for impurities because it possesses a direct optical bandgap and large natural abundances of nuclear spin-0 isotopes. The direct band gap allows efficient radiative transitions that can generate bright excitonic emission. Both single fluorine (F) donors [28] and single nitrogen (N) acceptors [22] have been optically isolated in this host material. Ensemble measurements have also revealed the potential for optical active spin qubits [11]. Recently, the growth of isotopically purified (Zn,Mg)Se/ZnSe quantum well structures was also demonstrated [29]. Spin purification of the host crystal further resulted in extended spin coherence times [30]. Moreover, donor-bound excitons in nanostructured pillars have been used to demonstrate indistinguishable single photon emission between two independent emitters [19], two-photon entanglement [20], and optical pumping of the donor spin [31].

Most studies on impurity-bound exciton emission have focused on the fluorine (F) impurity measurements, which possesses a smaller atomic radius compared to selenium (Se) atoms. Due to size difference between F and Se atoms, the crystal quality is worsened due to the defects generated at high doping concentrations. This effect is called self-compensation and limits the range of doping. On the other hand, chlorine (Cl) has an atomic radius closer to that of Se and is therefore more suitable as dopant with a low probability of self-compensation [32]. This enables Cl doping levels that cover a wide range of densities between 10^{16} cm^{-3} and 10^{19} cm^{-3}. But all past work on Cl impurity

bound exciton emission was in the large ensemble regime, and single Cl donor bound exciton emission has yet to be studied.

In this thesis, we will focus our attention to one particular type of impurity, Cl donors in ZnSe. We aim to study the optical characteristics of bound excitonic emission originated from Cl impurities, and show single photon emission from isolated Cl bound excitons. While doing that, we will also attempt to understand the spin properties of Cl impurity bound electrons. Lastly, we will demonstrate the fabrication of photonic devices in this material platform.

1.4 Thesis Outline

In Chapter 2, we will start with a short introduction of bound excitons in ZnSe where we will discuss how bound excitons are used to generate single photons. In Chapter 3, we will discuss the growth of the material and incorporation of Cl atoms to the ZnSe crystal. We will also discuss the motivation for using quantum wells and their effect on the radiative properties. In Chapter 4, we will detail optical characterization of radiative transitions of bound excitons. We will demonstrate the single photon emission from single Cl impurities. Following this discussion, in Chapter 5, we will discuss the energy levels, Zeeman splittings and allowed optical transitions of impurity bound electron. In the Chapter 6, we will report the formation of biexcitons from Cl complexes. We will demonstrate cascaded single photon emission from exciton-biexciton pairs. Finally, in Chapter 7, we will report our efforts to design and fabricate photonic crystal cavities in ZnSe platform.

Chapter 2: Bound Excitons in ZnSe

Isolated single impurities in crystals may host a bound electron that can serve as a spin qubit. They can also support bound excitons, excited electron-hole pairs, that can generate single photon emission. Combining these two capabilities in the same system is promising to realize spin-photon interfaces, which are fundamental blocks of spin based quantum computing. To achieve this broader goal, first, a number of fundamental steps must be realized. These are a) to isolate single impurities b) to realize efficient spin-photon interfaces c) to create interaction between multiple single qubits on the same chip.

The donor impurities at low doping concentrations can be used to isolate single photon emission and single spins. The donor bound electron generates a shallow potential trap for excitons, resulting in a donor-bound exciton emission localized at donor site. The donor bound exciton emission acts as a single atom-like quantum emitter that can emit single photons. The spin of the bound donor electron can serve as isolated single spin, that can be used as a quantum register.

To realize efficient spin-photon interfaces, impurities can be integrated in photonic cavities. These cavities serve as a medium to increase the interactions between electron spins and single photons.

To create interactions between multiple single qubits on the same chip, single photons

can be used. Photonic pathways such as waveguides enable the efficient transport of quantum information (encoded on single photons) on the different positions in the same chip. Hence, broad networks that allow the interaction of multiple localized spins can be realized.

Zinc Selenide (ZnSe) is appealing as the host crystal to host such impurities because it possesses a direct optical bandgap and large natural abundances of nuclear spin-0 isotopes [29, 33]. The direct band gap allows efficient radiative transitions that can generate bright excitonic emission. The existence of nuclear spin-0 isotopes allows to create spin-free background so that long coherence times can be achieved [30].

In this chapter, we will start with the discussion of the ZnSe crystal structure. We will discuss how Cl impurity is incorporated in the ZnSe crystal upon doping. Then, we will discuss the formation of bound excitons and their optical transitions.

2.1 Crystal Structure

Figure 2.1 illustrates the atomic structure of a ZnSe crystal with a single Cl impurity. In its intrinsic form, zinc and selenium atoms are arranged in a face centered cubic lattice where each zinc atom is surrounded by 4 selenium atoms. A single Cl impurity replaces a Se atom [34] when chlorine impurities are introduced into the lattice via in-situ doping or ion implantation. The Cl impurity serves as a neutral electron donor, consisting of the positively charged chlorine core and a bound electron, as shown in Figure 2.1.

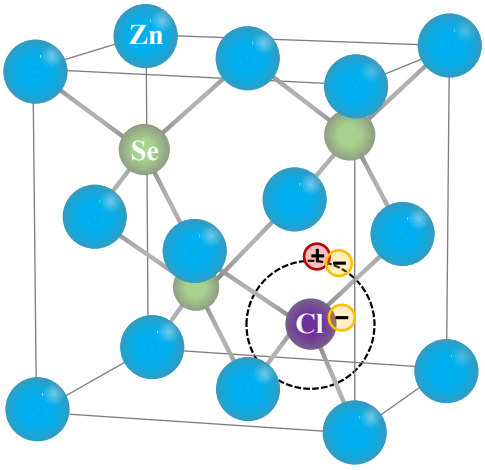

Figure 2.1: Crystal structure of ZnSe with a single Cl impurity substituting a Se atom.

2.2 Donor Bound Exciton State

A substitutional Cl donor in the ZnSe crystal provides a single electron. At the room temperature, this electron is in the conduction band due to the thermal energy. However, at sufficiently low temperatures, the attractive potential created by the donor atom can trap the free electron, hence the impurity electron becomes a localized bound electron at the impurity site. This donor-bound electron may serve as a stable electron spin qubit.

Figure 2.2 shows the energy level structure of the Cl impurity. Optical excitation above the ZnSe band gap produces free electron-hole pairs in the material. These electron-hole pairs, also called as free excitons, can become bound to the Cl impurity, and they form a bound state. This excited state is called the donor-bound exciton state and is shown as D^0X. Bound excitons can radiatively recombine back to the $1s$ ground state by

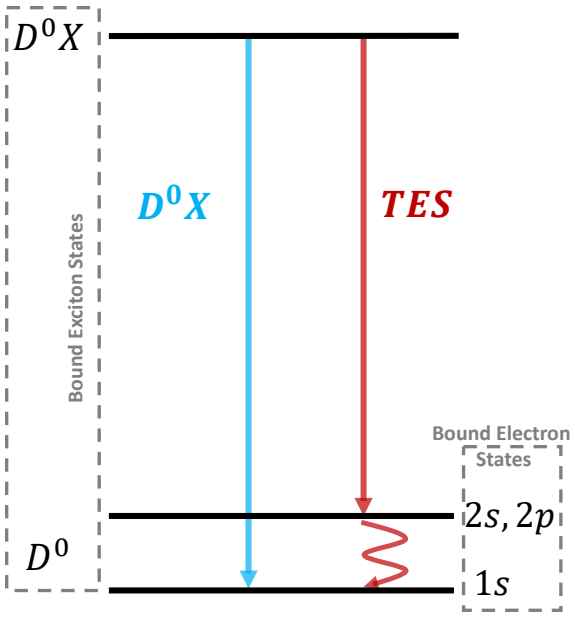

Figure 2.2: Energy band diagram showing the ground state (D^0) and excited state (D^0X), along with the bound exciton and two-electron-satellite emission, shown as blue and red arrow, respectively.

emitting a photon around 440 nm.

During the exciton recombination process, the bound electron can be excited temporarily to its higher energy $2s, 2p$ states and decay back to its ground state through an Auger recombination. If this happens, due to energy absorbed by the electron, bound exciton recombination produces a longer wavelength photon compared to D^0X. This emission is called as two-electron-satellite (TES) emission. TES signal can only be observed in the presence of the bound electron. Therefore, the observation of TES in the PL spectrum establishes the presence of the impurity-bound electron.

The binding energy of the donor-bound exciton can be approximated by the Hydrogenic model by using effective mass theory. Previous theoretical calculations show that the bound state formed by Cl impurity is a shallow state with a small binding energy, which is less than 7 meV. These bound excitons have Bohr radii of around 5 nm. These calculations will not be part of this thesis. Hence, we refer the reader to the references for detailed discussions [35].

Chapter 3: Material Growth

All samples studied in this thesis were grown by molecular beam epitaxy (MBE) process on the GaAs wafers. The quantum well structures are composed of ZnMgSe barrier layers and Cl doped ZnSe wells.

In this chapter, we will first discuss the layer structure of the samples, growth and doping process. Then, we will discuss the effects of the quantum wells on the optical properties of bound excitons.

3.1 MBE Growth

The growth of the material starts with a commercially available GaAs wafer. First, a thin (a few hundred nm) epi-layer of GaAs is grown on the GaAs wafer to achieve a clean and atomically flat surface. After the growth of the GaAs epilayer, the surface is passivated by arsenic cap-layer. Without exposing the surface to the air, the sample is transferred to the another chamber to continue the growth of ZnSe layers. During the transfer, ultra high vacuum is maintained to reduce the undesired impurity contribution from the background and to achieve defect-free growth. The details of the growth process can be found in the related literature [36–38].

Figure 3.1 shows the epitaxial layer structure of the sample used in this work. The

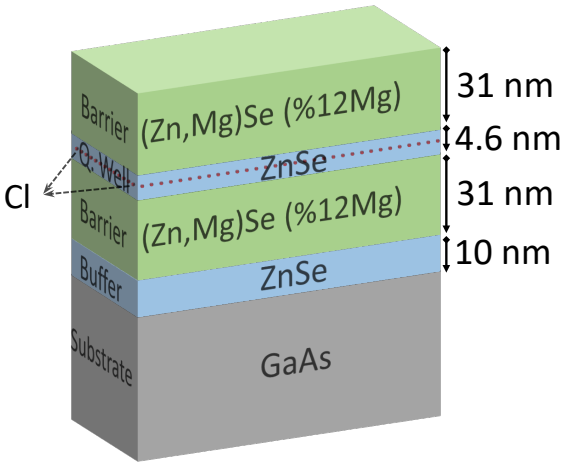

Figure 3.1: Layer structure of the grown material with in-situ doped Cl impurities in the ZnSe quantum well.

sample is composed of a 4.6 nm ZnSe quantum well embedded in a $(Zn_{0.88}Mg_{0.12})Se$ barrier on top and bottom each with a thickness of 31 nm. To achieve controlled doping of impurities while sustaining the high crystalline quality, we grow a thin Cl delta-doped layer in the middle of the ZnSe quantum well. The delta-doped layer has a Cl sheet concentration of approximately 10^9 cm^{-2}. The overall structure is grown on a GaAs substrate covered with a 10 nm ZnSe buffer layer.

The lattice mismatch between ZnSe and GaAs is between % 0.2 and % 0.4. The small mismatch allows two dimensional growth and high-quality epitaxial layers [39]. However, due to the small but existent lattice mismatch, the quantum well layer experiences a compressive strain.

3.1.1 Delta Doping of Cl Impurities

The delta doping of chlorine impurities is performed during the MBE growth of ZnSe/ZnMgSe layers. During the growth of the ZnSe quantum well, $ZnCl_2$ cracker cell is heated to 300 C$^\circ$ to dissociate Cl atoms. The precise control of doping time is achieved with the magnetic shutter that can be opened and closed in milliseconds resolution. Opening the shutter for short amount of time (usually 1 second) allows δ-doping of impurity atoms within a monolayer at the center of the well. The position of the Cl impurities within the well directly affects their binding energies due to the change in the strength of the quantum confinement. Limiting the doping profile to a single monolayer allows precise location of the Cl atoms (ignoring the diffusion), and it decreases the binding energy variations.

To calculate the doping concentrations in the δ-doped sample, we first measured the volume concentration (atoms/cm^{-3}) of impurity atoms in a uniformly doped epilayers with secondary ion mass spectroscopy (SIMS) and then we calculated the density of impurity atoms per monolayer.

3.2 The Effect of Quantum Confinement

Using quantum wells serves two purposes. First, due to the quantum confinement effect, the binding energies of the donor bound excitons are increased [40, 41]. Second, ZnMgSe barrier prevents the leakage of bound excitons from the the quantum well region, hence enhanced optical brightness can be achieved [42].

We define the binding energy of the bound exciton as the energy difference between

the free exciton emission in ZnSe (E_{FX}) and bound exciton emission of the impurity (E_{DX}). In the bulk, this binding energy ($E_{FX} - E_{DX}$) has been reported as 7 meV for Cl impurities [43]. Considering the similarity of Bohr radius (about 5 nm) of the excitons and quantum well thickness (4.6 nm), we expect both free exciton and bound exciton wavefunctions to be squeezed in the axis of the growth. This confinement causes an increase both in the binding energy of the free exciton ($E_g - E_{FX}$) and the binding energy of the bound exciton ($E_{FX} - E_{DX}$). Using the variational method for hydrogenic states, the increase in the binding energy can be estimated [44]. Using the quantum well has increased the binding energies by 2-3 times compared to the bulk values. This enhancement allowed us better separating the single bound exciton emission from the free-exciton spectrally.

Chapter 4: Radiative Properties of Single Bound Excitons

4.1 Introduction

Isolating impurities in ZnSe allows direct access to the atom-like transitions of single bound excitons. To understand the radiative properties of these transitions, the detailed characterization involving spectral and temporal measurements are required. Previous studies discussed in the Chapter 1 employed the nanopillars to isolate single F impurities. However, the bound exciton emission is susceptible to surface charge effects and material strain, both of which are modified due to the pillar geometry. Studying the optical transitions of donor bound excitons in an unstructured bulk material has greater importance to understand the both radiative and non-radiative properties. Nevertheless, to my knowledge, no previous studies have isolated single bound excitons in the bulk material to date.

Here, we optically isolate a donor impurity in a bulk material without using any nanostructure, and characterize the radiative properties of single bound exciton emission. Optical isolation of single bound excitons requires a sufficiently low density of impurity atoms and sufficiently large exciton binding energy. The latter is needed to separate bound exciton emission from the free exciton emission spectrally [40–42]. We achieve both of these requirements by using a quantum well that is delta-doped with a low concentration of Cl impurities, as discussed in Chapter 3.

In this chapter[1], we employ high-resolution optical spectroscopy techniques to study the radiative properties of single bound excitons. First, we start with photoluminescence measurements and discuss the spectral properties of the samples investigated. These measurements give us insight about the binding energies, inhomogeneous broadening and stability of the emission. Then, in section 4.3, we show results of photoluminescence excitation, and discuss the origin of the observed emission lines. In section 4.4 , we discuss the temporal dynamics of the emission by measuring the time-resolved photoluminescence. Then, in section 4.5, we measure photon correlations and demonstrate the single photon emission from the Cl bound excitons. Finally, in section 4.6, we discuss methods to tune the emission wavelength, and illustrate the temperature tuning. Our results demonstrate the isolation of single Cl impurities in ZnSe and provide complete characterization of bound exciton emission.

4.2 Photoluminescence Characterization

4.2.1 Measurement Details

To investigate the spectral properties at cryogenic temperatures, we mounted samples on an XYZ piezo stage and maintained the sample temperature at 3.6K in a closed-loop helium cryostat. During this study, we used two different cryostats, namely, Montana Cryostation CR-270 (Montana Instruments), and AttoDry 2100 (Attocube). Although both systems offer similar cryogenic capabilities, the latter allowed us to apply the magnetic field with the help of a built-in superconducting magnet.

[1]The results discussed here will be based on arXiv:2203.05748

To perform optical measurements in the wavelength region of the bound exciton emission, we built a confocal microscope system with free space and fiber optic components, working in the range of 400 nm - 550 nm. The optical setup was composed of an objective (NA:0.8), beamsplitters, waveplates and polarizers, filters, attenuators and fiber couplers.

We excited the samples with either 405 nm CW diode laser (Thorlabs) or frequency-doubled, tunable, 4-ps pulsed laser (Mira Optima 900P) with repetition rate of 76 MHz. The excitation wavelength of 405 nm corresponds to 3.06 eV, that is higher than both quantum well and barrier bandgap energies.

To spatially isolate individual impurities in the bulk material, we used confocal collection to a single-mode fiber. The single mode fiber has numerical aperture of 0.12. Using a small NA allowed us to filter the unwanted background signal coming from the neighborhood of the impurity emitter. We analyzed the photoluminescence signal with an imaging spectrometer (Princeton Instruments, SP-2750). The spectrometer is composed of an opening slit, a diffraction grating and nitrogen-cooled CCD. Narrowing the opening slit width to $30\ \mu m$ allowed us to achieve a spectral resolution of $15\ pm$.

4.2.2 Photoluminescence Spectrum

We start by analyzing the photoluminescence spectrum from the sample. We excite the sample with 405 nm CW laser that creates free electron-hole pairs (called free excitons) both in the quantum well and the barrier layers. The excitation scheme and creation of electron-hole pairs are sketched in the Figure 4.1.a. When the electron-hole pairs are generated in the quantum well, due to the attractive potential created by Cl impurities,

a single electron-hole pair may be trapped at a local impurity site and form a localized bound-exciton. The bound exciton state is not a stable state, hence it decays to its ground state by electron hole recombination. A single photon emission originates from this radiative recombination process.

There are three characteristic spectral features of the PL emission that is shown in Figure 4.1.b. The highest energy emission region of the spectra (labeled as FX, centered at 436.7 nm) is from the radiative recombination of free excitons in the quantum well. Close look up of this broad emission shows several sharp peaks within the bandwidth of FXline. These narrow lines are result of thickness fluctuations in the ZnSe quantum well. The second broad region denoted by X^{-}corresponds to the negatively charged trion state in the quantum well [45]. This emission is composed of 2 electrons-single hole pairs. In addition to these broader features, the distinct narrow feature (labeled as $\mathrm{D}^{0}\mathrm{X}$), originates from excitons bound to the single Cl donors.

Sharp and localized $\mathrm{D}^{0}\mathrm{X}$ lines are found around 15 meV away from the FX peak. As we move the position of the sample, we observe different localized lines appear in the spectrum at different spectral locations (mostly 5-20 meV away from FX), as opposed to constant energy FX and trion lines. Our main focus here will be on the location dependent narrow lines that are originated from the bound excitons.

To confirm that bound exciton emission originates from a two-level system with finite number of optical states, we perform intensity-dependent photoluminescence measurements. We record the spectrum at increasing excitation powers. Then, we fit the emission lines to a Lorentzian curve. Using the fitting, we extract linewidth and intensity of the emission for various excitation powers. We perform the same experiments with both pulsed and

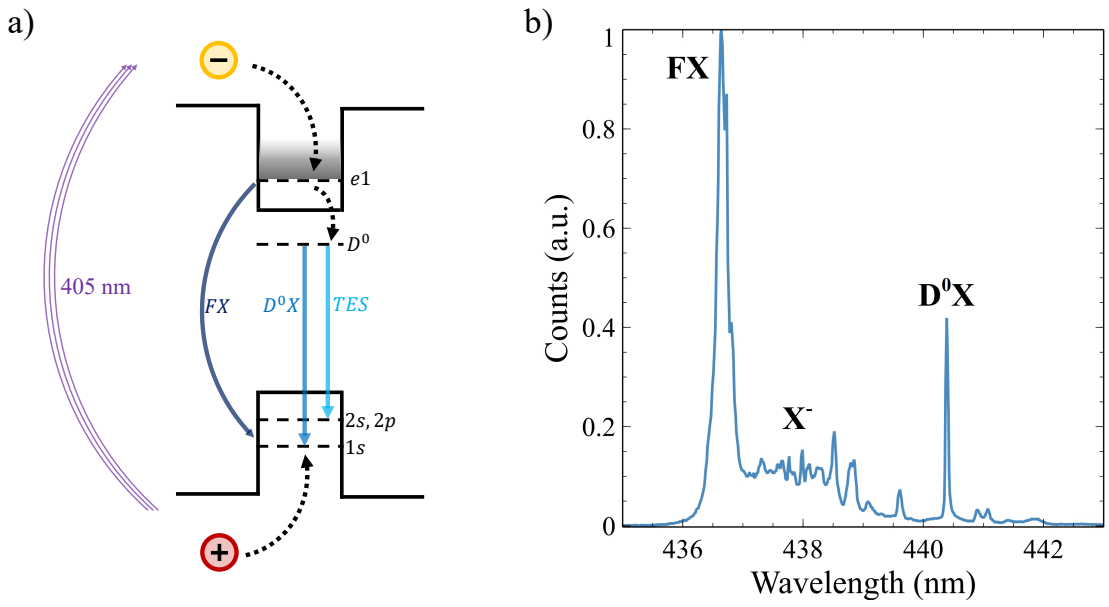

Figure 4.1: Photoluminescence response obtained with the above band excitation. a) Schematic illustrating the excitation and recombination mechanisms of the observed FX and D^0X lines. b) PL spectrum demonstrating free exciton (FX), trion (X^-) and bound exciton (D^0X) emission.

CW laser excitation. Both excitation schemes result in similar qualitative response. Here, we only discuss the latter for the sake of simplicity.

Figure 4.2.a shows the emission intensity of both free exciton and bound exciton line as a function of the pump intensity. The bound exciton line exhibits an intensity saturation at pump powers above $5\ \mu W$. In contrast, the free exciton line exhibits no saturation behavior in the applied excitation power range. The donor bound exciton state is composed of a single bound exciton, which can be modeled as a two-level system with a characteristic excited state lifetime. Due to finite number of optical states, the bound exciton emission saturates at low powers. On the other hand, we can create many free excitons within the excitation spot which causes FX emission to saturate at much higher pump powers. The emission intensity at the saturation is dependent on the brightness of the emitter.

The Figure 4.2.b shows the log scale power dependence of both curves for the low excitation powers, shown up to $20\ \mu W$. Fitting of both $\mathrm{D^0X}$ and FX lines up to $3\ \mu W$ shows linear dependence on the excitation power, with $P^{0.98}$ and $P^{1.06}$, respectively. The observed power dependence is consistent with the exciton power dynamics that is reported in the literature [46].

To show the effect of excitation power on the linewidth of the emission, we fit the bound exciton emission line to Lorentzian curve and extract the linewidth with respect to the pump power. The linewidth (calculated as FWHM) is shown in the Figure 4.3. At low powers, the linewidth is limited by the spectrometer resolution of 15 pm. At increasing powers, we observe a linear power broadening. The extrapolation to the zero power displays power-independent broadening as 0.01 nm (200 GHz). Although the value

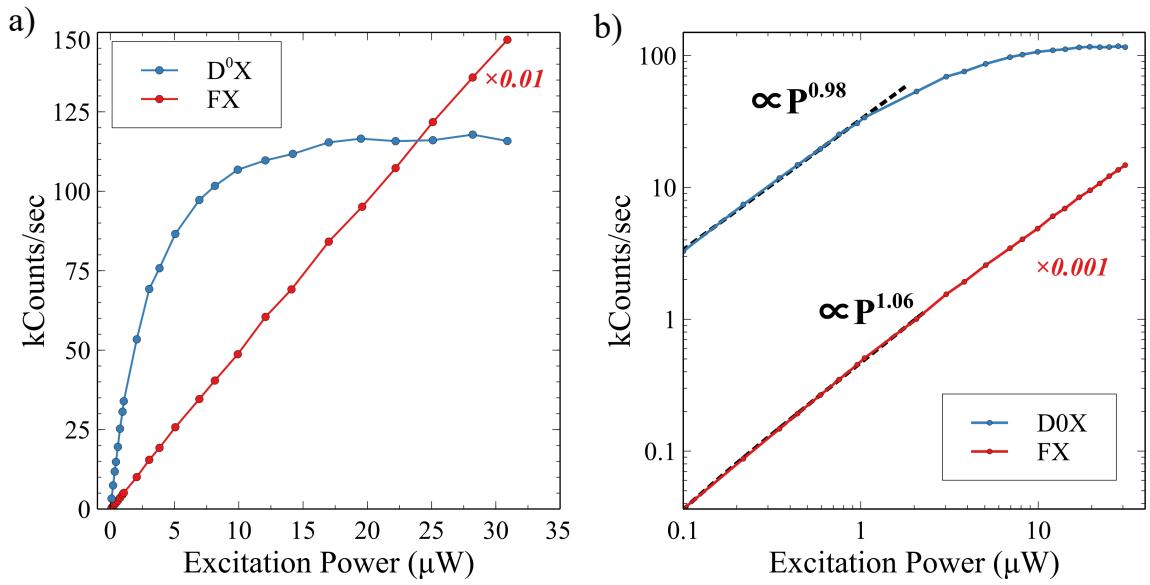

Figure 4.2: a) Power dependent intensity of bound exciton (blue) and free exciton (red), showing saturation of bound exciton lines. b) Power dependent intensity plotted in log scale for low powers up to 20 $\mu\ W$, showing linear dependence for both free exciton and bound exciton emission.

is close to lifetime limited linewidth of 5 GHz (which will be discussed in later sections), it is still non-negligible homogeneous broadening. This could be due to combined effect of charge instabilities and temperature induced effects.

4.2.3 Binding Energies & Inhomogeneous Broadening

Quantum interference between single photons generated by different triggered single photon sources forms the foundation of many optical quantum information processing schemes. To realize such quantum interference, one of the fundamental requirement is indistinguishability of the photons that are emitted by different photon emitters. To satisfy this requirement, one must ensure that emitted photons have same energies. The figure of merit that measures the similarity of emitted photons in terms of energy is called inhomogeneous broadening.

The attractive potential that bounds the exciton to the impurity site can be quantified as binding energy of the bound exciton. This is the energy needed to remove the bound exciton from the local impurity site, hence to make it free exciton. The binding energy can be calculated from the PL spectrum by measuring the relative relative energy difference between the free exciton (FX) and bound exciton ($\mathrm{D^0X}$) emission.

Measuring the distribution of emission energies of emitters from the same sample will reveal both the inhomogeneous broadening and the average binding energy of bound excitons. Figure 4.4 plots a histogram of the energies of 29 emission lines acquired at different locations. X-axis represents the binding energy (emission energy relative to the free exciton emission). The mean of the distribution is measured as 15 meV, which shows

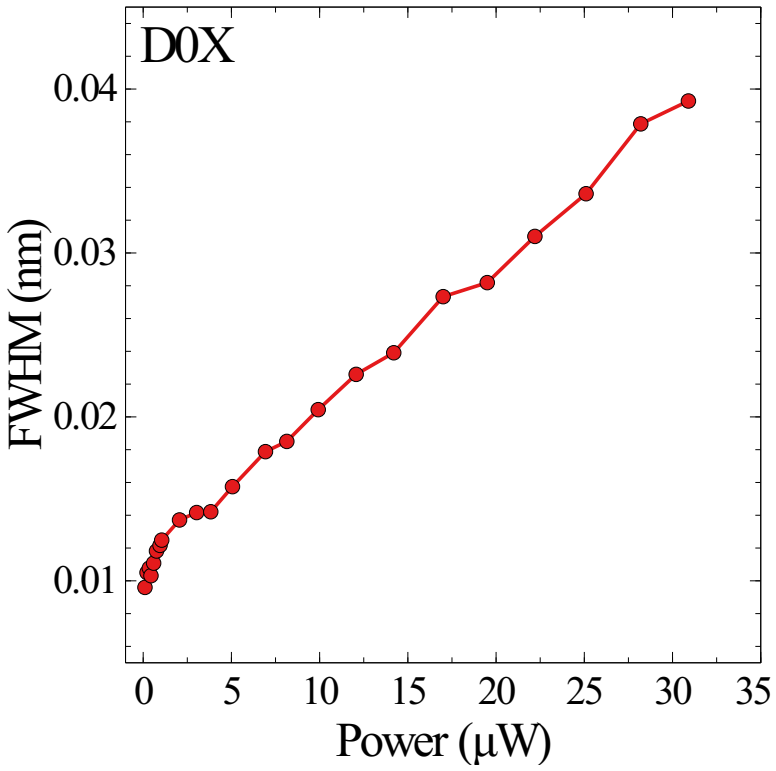

Figure 4.3: Linewidth of bound exciton line, extracted from Lorentzian curve fitting, showing a linear dependence on the excitation power. Extrapolation to zero power shows significant homogeneous broadening, that could be due to charge instabilities and temperature induced effects.

the average binding energy in the quantum well. This value is 2-3 times higher than reported bulk values (7 meV) [43]. The enhancement of binding energy allows better separation of FX and D^0X emission, and it is direct consequence of using quantum wells, as discussed in Chapter 3.

We calculate the standard deviation of the emission energies as 6 meV. The emission energy of each bound exciton depends on various factors such as the strength of quantum confinement and local strain. The strength of the quantum confinement will depend on the thickness of the quantum well and the position of the impurity in the quantum well [47, 48]. Both monolayer variations in the quantum well and diffusion of impurities in the growth axis may cause variations in emission energies, hence results in distribution of binding energies.

Although, the observed inhomogeneous broadening is better than epitaxial quantum dots [49], it is still significant compared to state of art impurity based systems [50]. However, these emitters exhibit very short lifetimes, which results in increased linewidths. For quantum interference applications, the ratio of the inhomogeneous broadening to the transform-limited linewidth is a better figure of merit to compare the emitters. Regardless, precise tuning of optical transition frequencies can be achieved with methods such as Raman tuning [51], magnetic field tuning [52], or strain tuning [53].

4.2.4 Stability

To investigate the stability of the emission, we monitored changes in the spectrum for both short time intervals, 10 seconds, and long time intervals, up to 7 hrs. For short

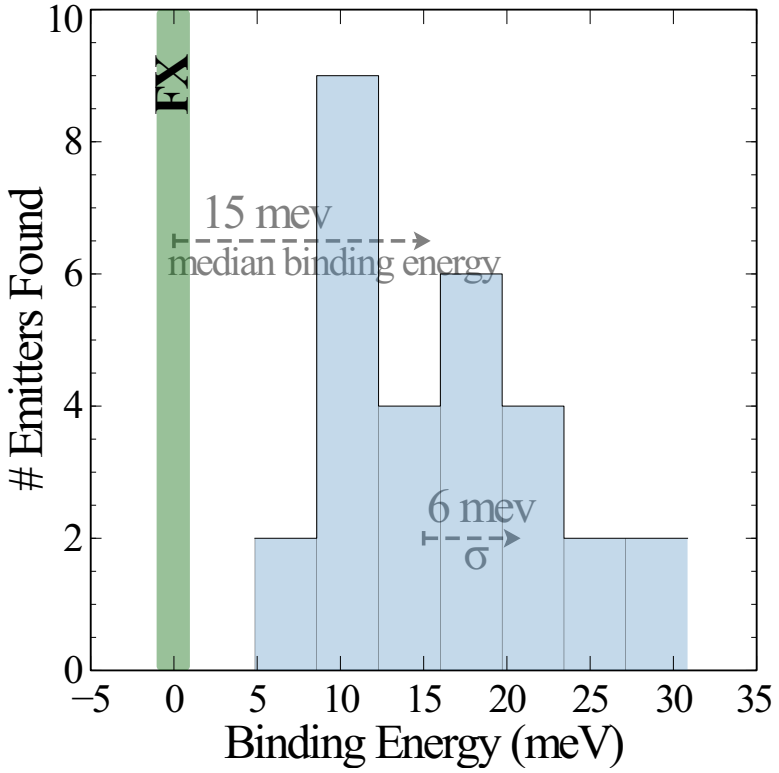

Figure 4.4: Histogram showing the distribution of binding energies of D^0X lines, with an average binding energy of 15 meV and a standard deviation of 6 meV.

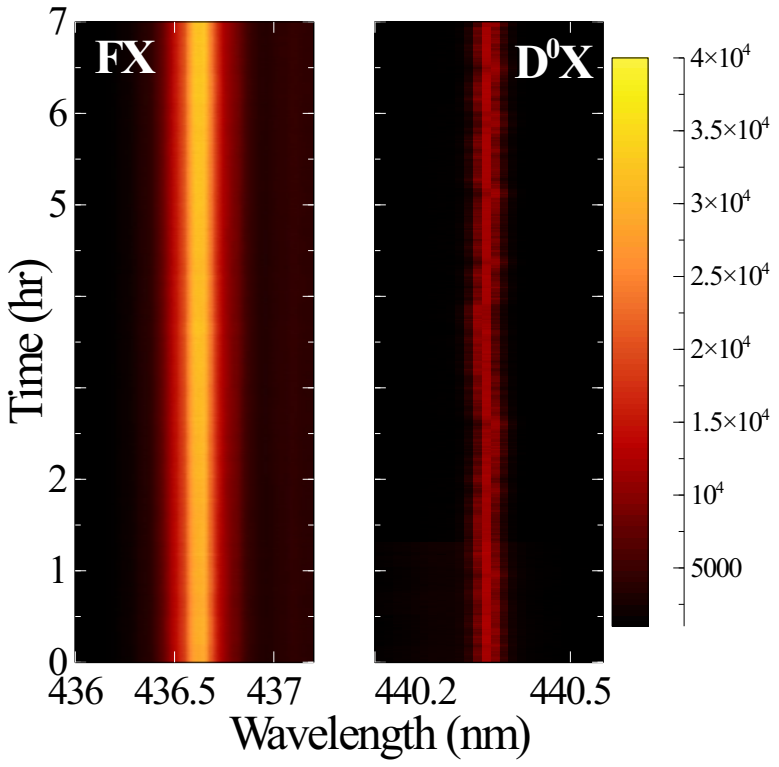

Figure 4.5: PL intensity recorded over 7 hrs showing the stability of the emitter.

term stability, we recorded the spectrum with an integration time of 1 ms for a total duration 10 seconds. The spectrum did not show any significant variation. Figure 4.5 highlights the long-term stability of the D^0X. The photoluminescence spectrum over 7 hours under continuous above barrier excitation is recorded. The emission displays no blinking, though slow spectral wandering is observed over a timescale of hours. We calculated the standard deviation of spectral wandering as 0.009 nm, which is in the same order of our spectrometer resolution. Nonexistence of blinking demonstrates of the stability of the emitter.

4.3 PLE Measurements

To verify that the observed D^0X emission originates from a bound state of the quantum well free exciton, we perform a photoluminescence excitation measurement. Figure 4.6.a demonstrates the excitation scheme. To avoid excitation of ZnMgSe barrier layers and selectively excite the ZnSe quantum well free excitons, we resonantly excite the FX line by tuning the pump laser on FX line. Resonant excitation efficiently creates free electron-hole pairs in the well. Since the probability of creating bound excitons depends on the concentration of free excitons, efficient generation of free electron-hole pairs in the well results in enhanced brightness from the bound exciton.

We use a tunable laser with a fixed pump power of 100 nW. We tune the laser emission over the free exciton line and monitor the emission from a D^0X line. During this measurement, we also inject a weak above-band laser (about 3 nW at 405 nm). At this power, the above-band laser produces negligible photoluminescence. However, it creates a population of electron gas in the barrier that tunnels to the quantum well and maintain the electron-rich charge configuration in the quantum well [54–56]. In the absence of above band laser, the quantum well has hole-rich configuration, which prohibits the observation of bound excitonic emission.

Figure 4.6.b shows the photoluminescence excitation spectrum of a D^0X line as we tune the pump laser over the free exciton line. We observe strong emission from the D^0X line when the laser is resonant with the free exciton. This enhancement suggests that free excitons in the quantum well non-radiatively relax to form donor-bound excitons at the impurity.

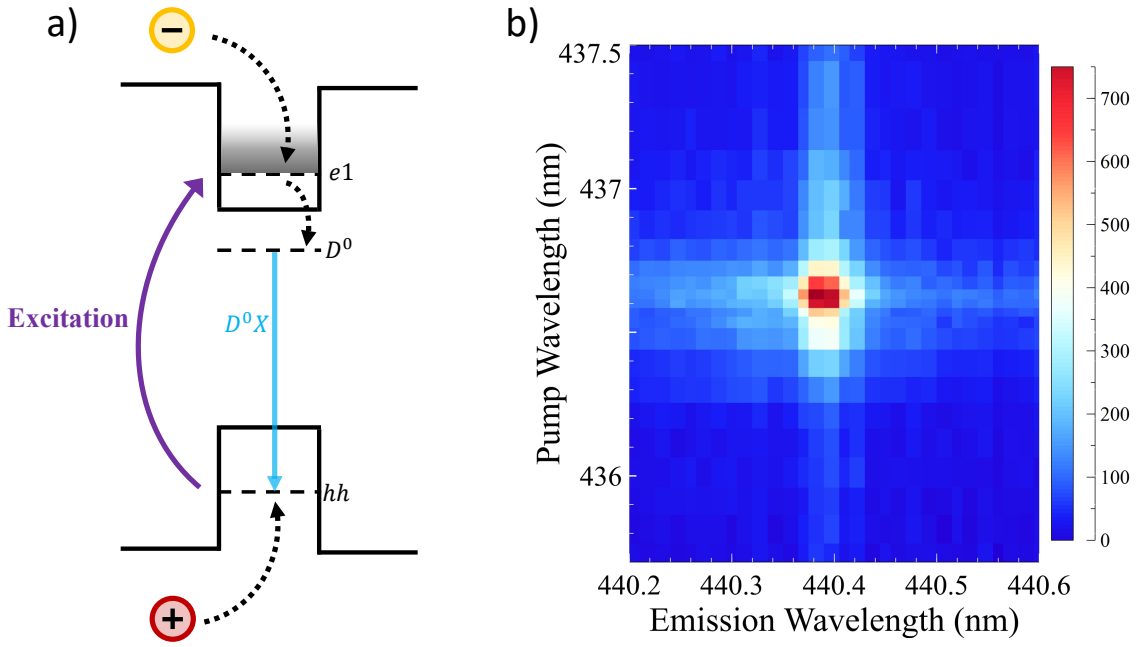

Figure 4.6: Photoluminescence excitation a) Schematic illustration showing how resonant excitation of FX line creates bound excitons. b) PLE spectrum of bound exciton line obtained by tuning the pump laser over the FX line.

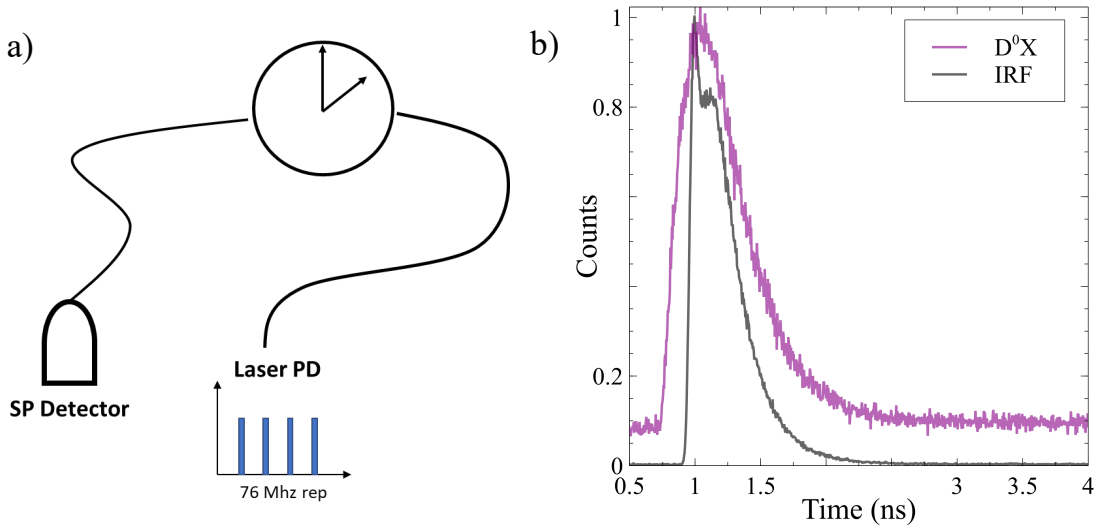

Figure 4.7: Time resolved lifetime measurement setup a) The measurement configuration to characterize the timing response of the measurement system. b) The instrument response function (IRF) showing the limited time resolution caused by detector timing jitter.

4.4 Lifetime of Emitters

To characterize the donor-bound exciton state's lifetime, we perform time-resolved fluorescence measurements. To excite the emitters, we frequency-double a tunable, mode-locked, Ti-sapphire laser (Mira 900P, Coherent) by using a nonlinear crystal. This configuration allows us to get 4 ps pulses at 405 nm with a repetition rate of 76 MHz. We use single photon avalanche photodiodes (PDM Detector, Micro Photon Devices) and a time correlated single photon counting module (Picoharp 300, Picoquant) to record the photon arrival times relative to the laser pulse, shown in Figure 4.7.a.

The detector time jitter is the limiting factor to measure the fast dynamics. To characterize the limits of our measurement capability, we first record the instrument response function of the overall system at our measurement wavelength. To do that, we tune the excitation laser to the bound exciton emission wavelength (440 nm), and record the each detector pulse with photon detectors. Since the laser pulse is very short, it can be approximated as delta function, hence the histogram of detection times shows the impulse response, shown in Figure 4.7.b.

To mitigate the slow timing response of detectors, we reconvolved (EasyTau software, Picoharp) the detector impulse response recorded at the emission wavelength with custom defined decay function. We extracted the parameters of decay function by fitting the reconvolved function to the measured data. Extracted data shows a biexponential decay, with a dominant fast decay time of 192 ps and a weak contribution from a slower component with a decay time of 2.49 ns. Figure 4.8 shows the histogram of photon arrival times obtained from a single bound exciton along with the bi-exponential decay fit.

To investigate the origin of biexponential decay, we repeated the same experiment at higher temperatures. Although only %4 of photons are originated from the slow component at 4K, the contribution of slow decay to total photons rises to %24 at 60K. The origin of the slow component may be caused by the repopulation of the D^0X state from longer-lived nearby trapping states and is a matter of further investigation.

The fast decay time of donor bound exciton transitions is an indicator of bright emission. Combined with small inhomogeneous broadening, these well-defined and fast emissions are making Cl impurities attractive candidates as efficient single photon source.

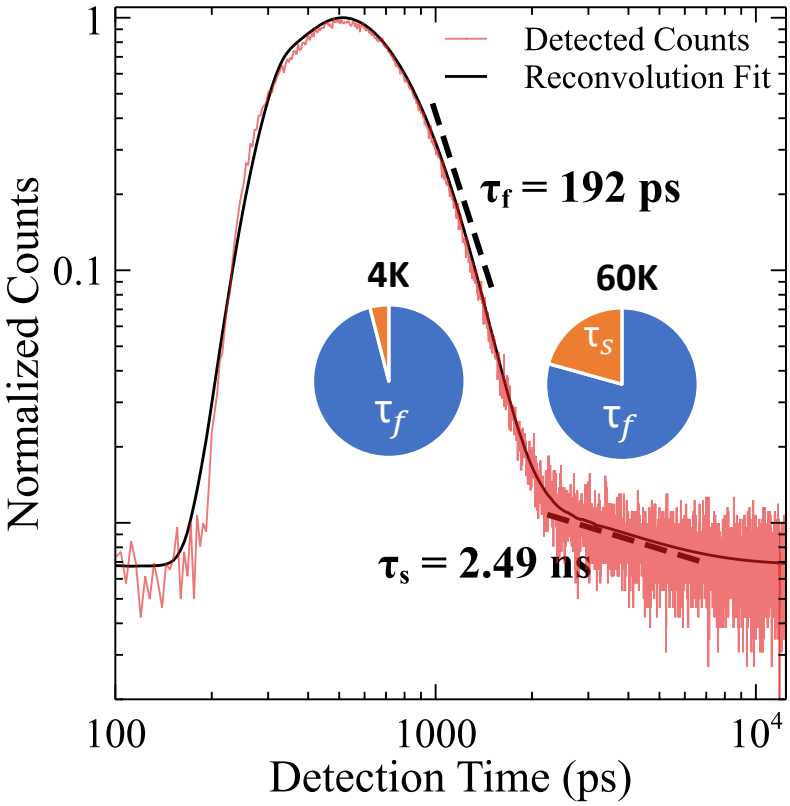

Figure 4.8: Time-resolved photoluminescence measurement, showing biexponential decay with dominant fast decay component of 192 ps and slow decay component of 2.49 ns.

4.5 Single Photon Generation

To optically isolate single bound excitons, we aimed to limit doping concentration to allow only 1-2 impurity per the optical diffraction spot. The delta doping of Cl impurities allowed locating the emitters at the center of the quantum well in the growth axis. The barrier layers serves the purpose of preventing the carrier diffusion into to the lower bandgap material,i.e. GaAs substrate. The lateral distribution of emitters are random, but we can search for them by laterally scanning the sample. Hence, by choosing low doping concentration, we achieve the isolation of individual emitters without need for further nanostructuring.

In order to demonstrate the single-photon emission, we perform second-order photon correlation measurements. We use a frequency-doubled Ti:Sapphire laser emitting at 405 nm with a pulse repetition rate of 76 MHz to excite the emitters. We efficiently collect the emitted photons from the sample by using a high NA objective (NA:0.8). Then, we couple to collected light to a single mode fiber (NA:0.12) to spatially isolate individual emitters.

To spectrally filter the narrow $\mathrm{D^0X}$ emission lines, we use a monochromator and a narrow slit. The monochromator grating disperses the collected light, and the variable-width slit allows us to filter wavelength region of interest by tuning the grating angle and slit-width. This configuration allows us both tuning the center wavelenth and bandwidth of filtering. After the monochromator, we place a free-space 50:50 beam splitter to split the incoming photons into two identical paths. Each path has identical single photon detectors (PDM Detector, Micro Photon Devices) which are connected to time correlated

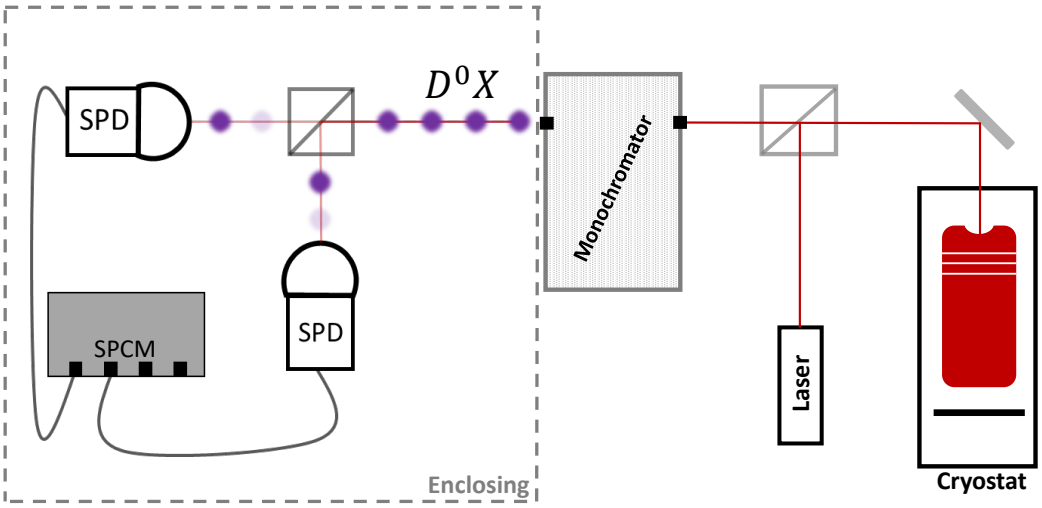

Figure 4.9: The schematic of the setup to measure the autocorrelation function from the D^0X line. First, the collected light is filtered with the monochromator, then photons originated from bound exciton emission are sent to the identical detectors. We enclose the detectors to avoid the room light contribution.

single photon counting module (Picoharp 300, Picoquant). During the measurement, we enclose the photon detectors to avoid any unwanted light. The Figure 4.9 shows the schematic of the setup.

Photon correlations can be calculated by measuring the photon arrival times between detectors. In the presence of incoming single photons, we expect to see a dip in the coincidence counts, because the photon will either be detected in the horizontal or the vertical detector. This results in photon anti-bunching for zero time delays between detectors.

To observe the photon anti-bunching, we recorded the histogram of coincidences for 60 hours. To ensure the stability of the long integration measurements, we constantly monitored the detector counts and spectrum, and fixed any sample shifts. The Figure 4.10.a shows the raw counts of the second-order auto-correlation measurements performed on the single line. The photon anti-bunching is clearly observed for the zero time delay.

The spectral filtering allows us to remove the unwanted photons coming from the nearby wavelengths. However, there are two more noise sources that contribute to the coincidence histogram. The first one is the detector dark counts. The second one is due to the the background counts that are within the bandwidth of the monochromator.

To remove the contributions due to detector dark counts and background emission, we post-processed the data. The detector dark counts are not correlated with the laser pulse. Hence, they result in uniform rise in the histogram counts. To remove the dark count contributions, we calculate the average of the uniform base and remove it uniformly from coincidence counts.

To remove the background emission contribution, we first quantified the emitter and

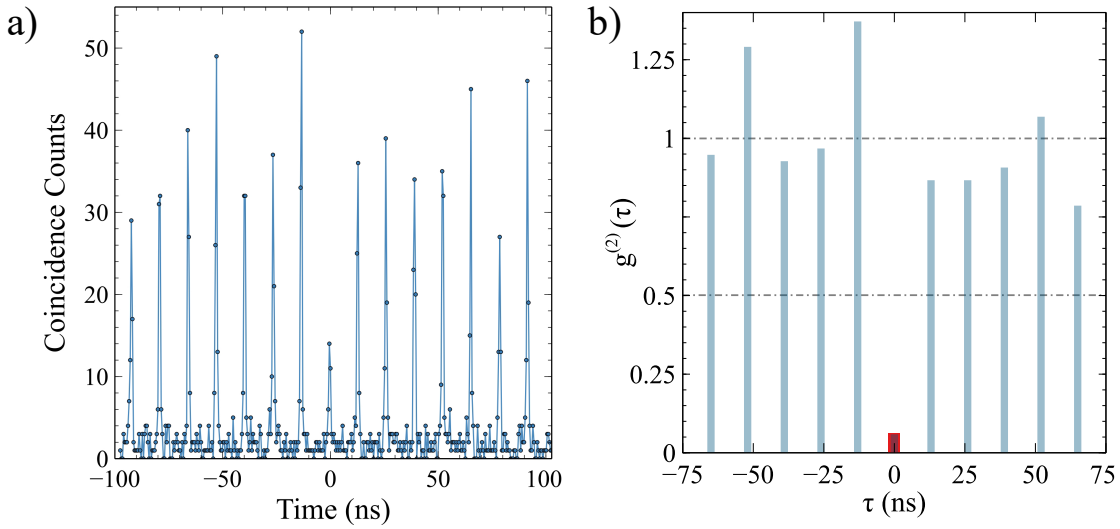

Figure 4.10: a) Coincidence counts of two detectors with variable time delay, obtained with 60 hours of integration, showing emitted photons are single. b) Noise corrected second-order auto-correlation function obtained from the single line, demonstrating almost perfect photon antibunching.

background counts on the detectors. The total counts in detector 1 and 2 can be written as $D_1(t) = S_1(t) + B_1(t)$, $D_2(t) = S_2(t) + B_2(t)$, respectively. $S(t)$ represents the pure emitter counts, whereas $B(t)$ represents the background. Assuming that background emission has Poisson distribution, it will result in a uniform pulse train in the histogram. However, we expect $S(t)$ to show perfect antibunching, hence it will result in a perfect pulse train except for zero time delay. Here, the counts measured at non-zero time delay pulses will be determined by $D_1(t) * D_2(t)$ but only the contribution coming from $S_1(t) * S_2(t)$ is actually emitter counts. Here, we take the average of non-zero time delay pulses, lets say N, and calculate the numeric contribution of background by $N * (D_1 * D_2 - S_1 * S_2)/(D_1 * D_2)$. Finally, we extract this background contribution uniformly from all pulse trains including the zero time delay pulse. After the noise correction [57], the second-order correlation exhibits almost perfect anti-bunching with $g^2 = 0.06$ (Figure 4.10.b), which confirms that the emission line corresponds to a single photon emitter.

4.6 Temperature Tuning of the Emission

We demonstrated, in Section 4.2.3, that Cl bound excitons from the same sample exhibited small inhomogeneous broadening with standard deviation of 6 meV. However, to increase the probability of frequency matching of the emission from individual donors, various tuning mechanisms such as electrical tuning, thermal tuning and strain tuning can be employed. Here, we will limit ourselves to thermal tuning of emitters.

Figure 4.11.a shows the PL emission of both D^0X and FX lines with increased sample temperatures up to 70K. By increasing the temperature in this range, we tuned

the emission by 3.5 meV without much sacrificing from the integrated brightness. At temperatures higher than 60K, we observed a significant temperature broadening (Figure 4.11.c), which limited our tuning range.

Figure 4.11.b shows the shift of both FX and $\mathrm{D^0X}$ lines with respect to sample temperature. Both curves show a similar temperature dependence, proving that wavelength shift is due to change in the band gap of the material at increased temperatures [58, 59].

We achieved tuning the emission more than half of the standard deviation of the inhomogeneous broadening. Although our results show that temperature tuning can be employed to some extent to tune the emission of emission from the different emitters, other tuning mechanisms such as stark shift or local strain tuning may be investigated for better tuning capabilities.

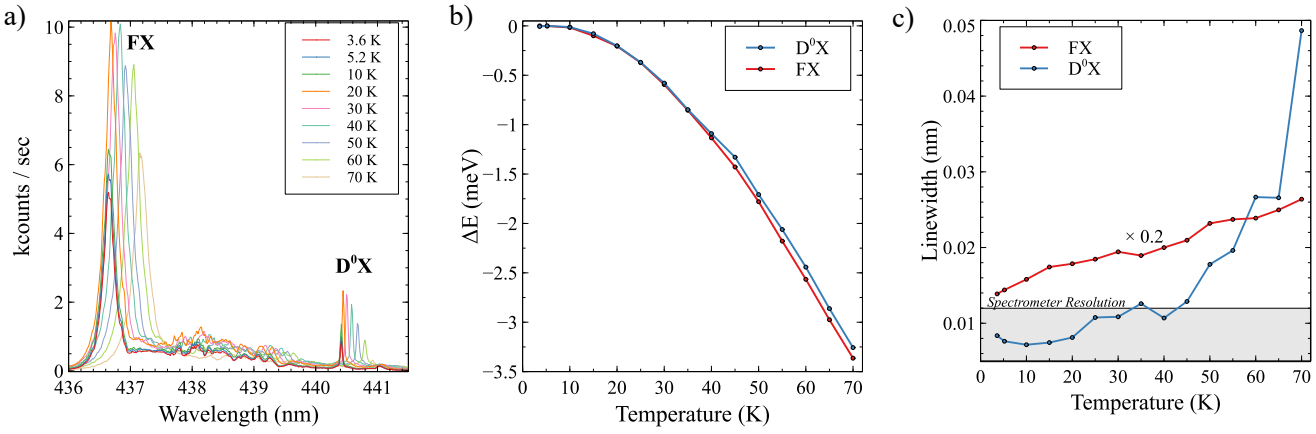

Figure 4.11: Temperature tuning of the emission. a) PL spectrum obtained at increasing sample temperatures up to 70K. b) The relative shift of emission energies of FX and D^0X lines from the 3.6K values, showing a similar temperature dependence for both curves. c) Temperature dependent linewidth showing that significant broadening starts at 60K

4.7 Summary

In this chapter, we optically isolated single excitons bound to the Cl donor atoms in ZnSe quantum wells. We observed clear saturation of emission intensity at increased excitation powers, demonstrating the finite optical states of bound excitons. We confirm the stable single photon emission by observing a clear photon antibunching. The fast radiative recombination time below 200 ps demonstrates the potential for high brightness. Our results establish Cl bound excitons as bright and stable single photon sources.

Chapter 5: Spin States of Bound Electrons

The realization of spin-photon interface requires robust and optically accessible spin qubits. The bound electron of an impurity can serve this purpose because ground state of the bound electron possesses spins that can be employed as a qubit. In this chapter[1], we will study the both ground and excited states of electron donor bound to the Cl impurity by using magneto spectroscopy techniques.

In a neutral donor system, at cold temperatures, we expect the donor electron to be bound to the impurity and become localized at the impurity site. Before discussing the spin states, we will first start with resonant excitation of bound excitons and observing for the existence of two-electron-satellite emission. The presence of TES signal allow us to establish the existence of the bound electron.

Under no external magnetic field, neither ground nor excited states show significant fine structure. However, the degenerate spin states split in energy by increasing the magnetic field, further allowing selective optical access to desired qubit states [60]. In the rest of the chapter, we will discuss how degenerate energy states of single electron system will split under external magnetic field. Based on this discussion, we will discuss the selection rules that govern the allowed optical transitions. In the following sections, we

[1] A manuscript is under preparation discussing the results from this chapter.

will introduce our measurement setup to characterize the system. Magneto spectroscopy results will unleash the detailed level structure under both Faraday and Voigt magnetic field. Our results will verify the presence of spin qubit states from Cl bound electrons in ZnSe quantum wells.

5.1 Two-Electron Satellite Emission

Optical excitation above the ZnSe band gap produces free excitons in the quantum well. These excitons can become bound to the Cl impurity, forming an impurity bound exciton state $\mathrm{D^0X}$. This state can radiatively recombine back its ground state by emitting a photon around 440 nm. During this process, the bound electron can absorb some energy, can be excited to higher orbital states such as 2s,2p states. Due to this energy lost, bound exciton emission is redshifted by around 20 meV. This emission is known as two-electron-satellite (TES) and shown in Figure 2.2.

The Figure 5.1 shows the PL signal obtained with a weak above-band laser and varying power of resonant pump laser tuned at the $\mathrm{D^0X}$ line. Two-electron-satellite (TES) emission 19.6 meV below the $\mathrm{D^0X}$ line emerges, and its intensity increases as we increase the resonant pump power. Satellite emission appears lower in energy by an amount equal to the spacing of the n=1 and n=2 D^0 electron orbitals determined by a Hydrogenic donor model [43]. The weak nature of this emission is due to the predominant relaxation of D^0 state to 1s ground state. However, there is a finite probability of relaxation to any of the excited (2s, 2p, etc.) states as discussed in the Figure 2.2 . To be able to observe this low-efficiency emission in the existence of other broad features, we used low-power excitation

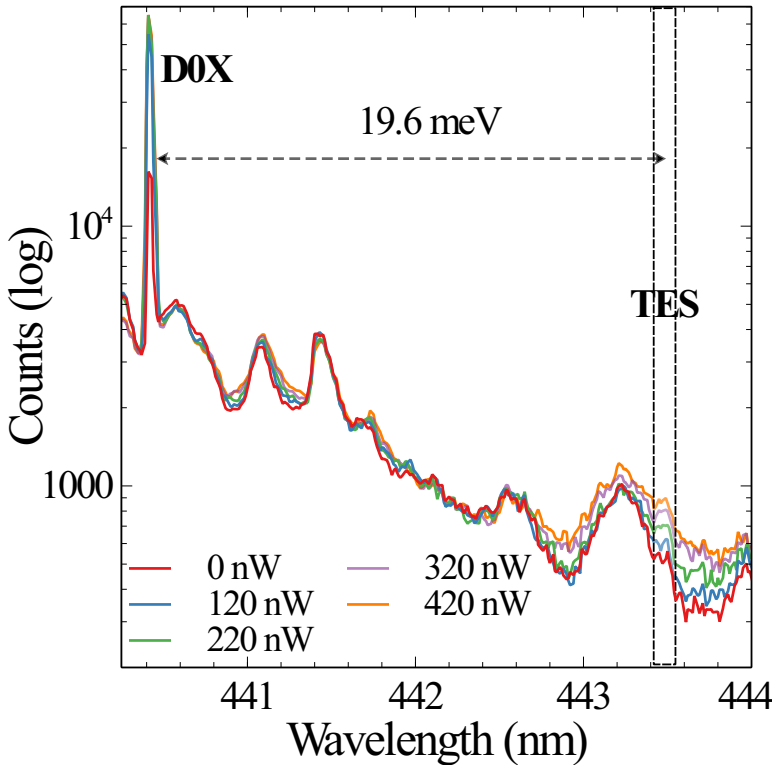

Figure 5.1: Spectrums showing the TES line with increasing resonant pump. power

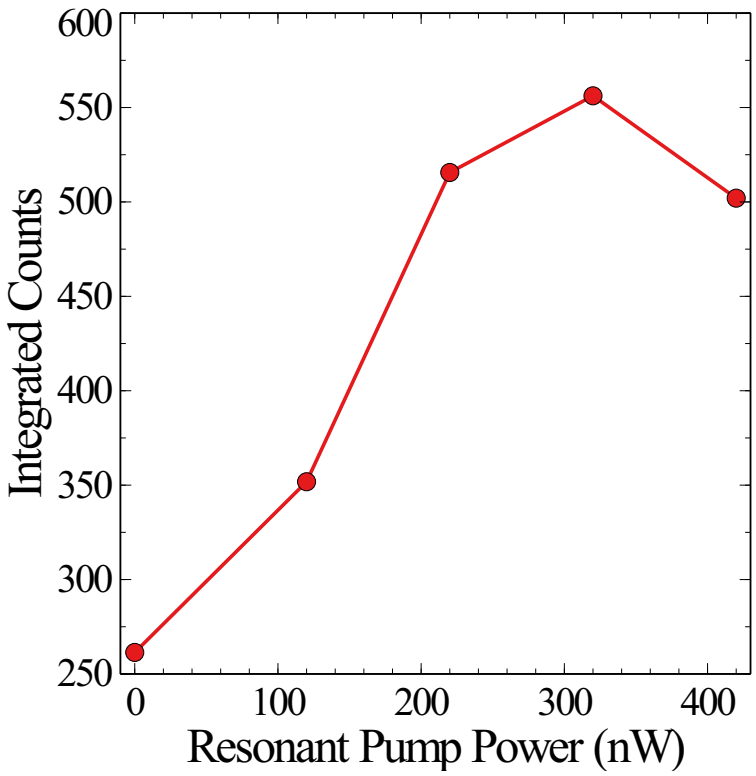

Figure 5.2: Background corrected and integrated counts from dashed spectral window showing saturation of TES line with increasing pump power.

and long integration times (60 sec). The background corrected integrated intensities with increasing pump power shows saturation, shown in Figure 5.2. The observation of two-electron satellite emission supports the presence of an impurity-bound electron [43, 61], hence potential spin qubit.

5.2 Donor Electron Energy States under Magnetic Field

Energy levels and optical selection rules of electron in an atom can be described by four fundamental quantum numbers [8]: the principal quantum number (n) (describes energy eigenstates), angular quantum number (l) (describes the orbital angular momentum), magnetic quantum number (m_l) (describes the orientation of orbital), and the spin quantum number (m_s).

Due to spin-orbit interaction, both the angular momentum (l) and spin momentum (m_s) can contribute to the total angular momentum (J), which can be written as:

$$J = l + s, \tag{5.1}$$

It semiconductors, electrons in the conduction band exhibit s-like orbital wavefunction while holes exhibits p-like orbital wavefunction. Hence, we can assume that $l = 0$ $(m_l = 0)$ for electrons and $l = 1$ $(m_l = -1, 0, 1)$ for holes while both have $s = 1/2$ $(m_s = -1/2, 1/2)$. The total angular momentum for s orbitals becomes $J_s = 1/2$ and for p orbitals, $J_p = 3/2$ [62].

Considering the spin-orbit coupling, the total angular momentum can have for s-like states $m_j = -1/2, +1/2$ and for p-like states $m_j = -3/2, -1/2, +1/2, +3/2$.

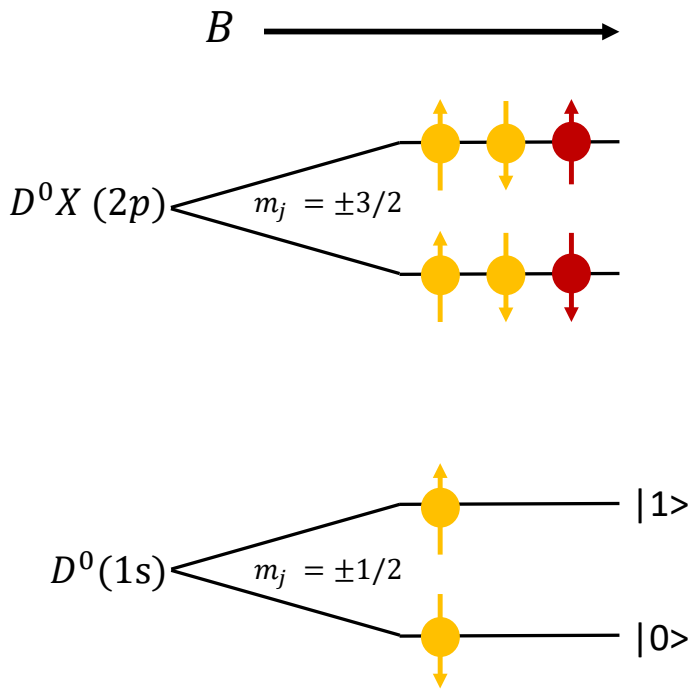

Figure 5.3: Energy levels and spin configurations of the (ground) bound electron and (excited) bound exciton states.

When an external magnetic field is applied, these degenerate energy states will become non-degenerate due to different coupling ratios to external magnetic field. Due to this perturbation, lifted degeneracy will result in energy differences between the states. In our MBE grown sample, ZnSe/ZnMgSe on GaAs exhibits internal strain that lifts the degeneracy between light-hole (LH) and heavy-hole (HH) states in the valence band. Therefore, heavy-hole states and light-hole states will exhibit $m_j = -3/2, +3/2$ and $m_j = -1/2, +1/2$ respectively.

The Figure 5.3 demonstrates how degeneracy is lifted upon the external magnetic field. In the neutral charge configuration, where bound electron resides in the valence band, there are two possibilities, as $m_j = -1/2$ and $m_j = +1/2$. These two states form the basis for the electron spin qubit. In the excited state, electron-hole pair binds to the the electron, hence bound exciton is composed of 2 electrons and 1 holes. In this state, electrons form a singlet, and total angular momentum is determined by the hole of electron-hole pair.

Due to the internal strain supplied by the quantum well, HH and LH states become already nondegenerate even without any magnetic field [62]. Also, it is shown that HH transitions are more profound with higher probability of recombination. In fact, PL measurements showed only the emissions related to HH states. Therefore, we limit our attention here only to heavy-hole (HH) transitions.

5.2.1 Energy Splitting

Under the magnetic field, magnetic moment interacts with the magnetic energy, and the interaction energy can be written as

$$E = -\vec{M} \cdot \vec{B_z} = g\mu_b m_s B \tag{5.2}$$

where g is the Landé g-factor of a free electron, μ_b is the Bohr magneton. Depending on the electron/hole spin quantum number, the energy difference between states can be calculated.

In the real crystal, there are some considerations must be taken into account to

model the energy splitting. First of all, due to crystal potential, effective g-factors will be different than free space values. Secondly, electron and hole exhibits different g-factors which are also dependent on the temperature and crystal conditions such as defect density and growth conditions [63]. Due to such differences, although the numerical values may differ from the theoretical calculations, qualitative discussion still will be valid. We will use the experimental magneto spectroscopy data to extract the effective g-factors for both holes and electrons.

5.2.2 Optical Selection Rules

As discussed in the previous section, the ground state electron has angular quantum number $l = 0$, so it does not have any orbital angular momentum, and orbital shows perfect spatial symmetry. Hence, the spin of ground state electron will align itself to the applied magnetic field, independent from the axis. However, excited state hole has p-like orbital with $l = 1$. P-orbitals, unlike s-orbitals, do not posses perfect spatial symmetry. Hence, their reaction to magnetic field will differ depending on the field direction.

In the absence of quantum well confinement, the hole wavefunction can have any value of $m_l = -1, 0, 1$. However, since quantum well has thickness around the Bohr radius of exciton, the quantum confinement will lead the orbital wavefunction to spread in the in the lateral direction.

When the magnetic field is applied in the growth direction (Faraday configuration), hole spin will be oriented in the growth direction. However, when magnetic field is in-plane (Voigt configuration), the magnetic field will compete with the quantum well

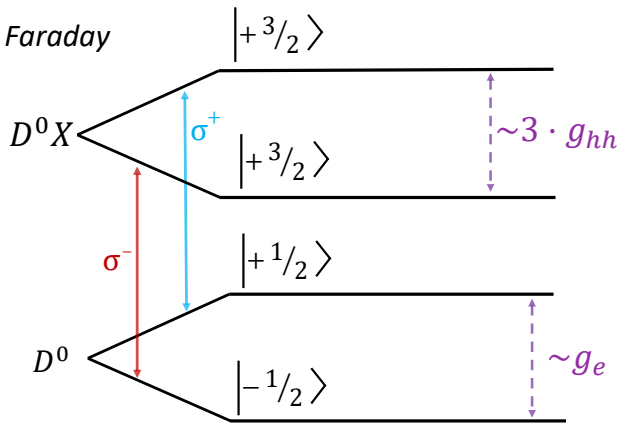

Figure 5.4: Zeeman splittings of ground and excited states of bound exciton, along with optical transitions under Faraday magnetic field.

confinement to orient the hole spin. This competition causes a mixture of the hole spin states in the $\mathrm{D^0X}$, allowing additional optical transitions [60].

Conservation of angular momentum only allows radiative emissions if $\Delta m_J = \pm 1$ between the transitions. Figure 5.4 shows the allowed optical transitions in Faraday geometry. In this configuration, two orthagonal circular polarizations become allowed.

Figure 5.5 shows allowed optical transitions in Voigt geometry. In this configuration both excited states demonstrate linearly polarized transitions with each of ground state levels. Optical lambda system formed between transitions allows optical access for manipulating spin, hence forms the basis for control and readout for spin qubits.

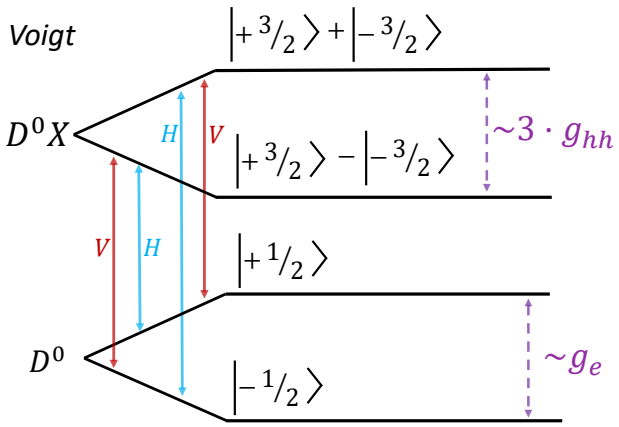

Figure 5.5: Zeeman splittings of ground and excited states of bound exciton, along with optical transitions under Voigt magnetic field.

5.3 Magnetospectroscopy Experiments

We have discussed the theoretical background for the optical transitions in Faraday and Voigt geometry. Here, we provide the experimental demonstration by analyzing magneto-PL emissions from single bound excitons.

5.3.1 Measurement Setup

To characterize our samples under an external magnetic field, we perform polarization resolved Pl measurements. We keep the samples in the closed-loop helium cryostat (Attocube) equipped with an an objective lens and XYZ piezo nano-positioners (ANPx51/LT). To apply static magnetic fields up to 9T, we use cooled superconducting magnets. First, we collect the PL signal with high-NA objective. Then, using quarter wave plate, half

wave plate and polarizer, we set the desired polarization for the collection. Using polarization optics at different angle configurations allows us to measure the PL at different polarization basis.

The superconducting magnet has capability to apply magnetic field only in one axis. To switch between Faraday and Voigt configurations, we change the sample holder and objective configuration. The rotating the sample holder and replacing the objective accordingly allow us accessing the sample optically from the top, without changing the external optics. The Figure 5.6 shows a sketch of both configurations, along with picture of Attocube insert that holds the objective and sample stage.

5.3.2 Faraday Magnetic Field

The optically allowed transitions in this configuration are presented in Figure 5.4. The total spin of the bound exciton ground state is given by the single spin-1/2 electron. In the bound exciton excited state, the donor electron forms a spin-singlet with the electron of the exciton, giving a total spin determined by the spin-3/2 heavy hole. For increasing magnetic field, two orthogonally polarized circular emission lines emerge as expected, shown in Figure 5.7.

Two circular polarized photon emissions; σ^+ and σ^- circular polarization, can be distinguished by using a quarter-wave plate with the fast axis at +45° or -45° angle. Spectra indicated by solid (dashed) lines are recorded for σ^+ (σ^-) polarization with increasing magnetic field intensities as shown in Figure 5.7. The energy difference of the two allowed transitions is proportional to $g_{eff} = g_e - 3g_{hh}$. From the observed energy

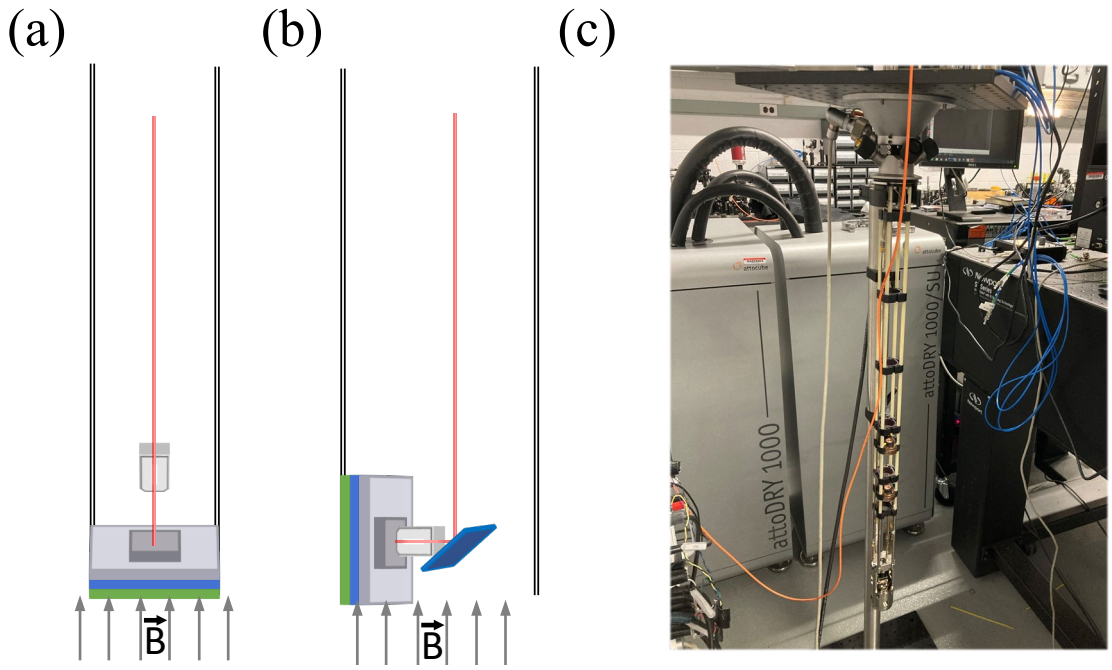

Figure 5.6: Optical setup to measure PL under the applied magnetic field. a and b) Schematic demonstrating the configuration of the insert (composed of XYZ stage, the sample, and the collection lens) for Faraday (Voigt) field measurements. c) The picture of the Attocube sample insert.

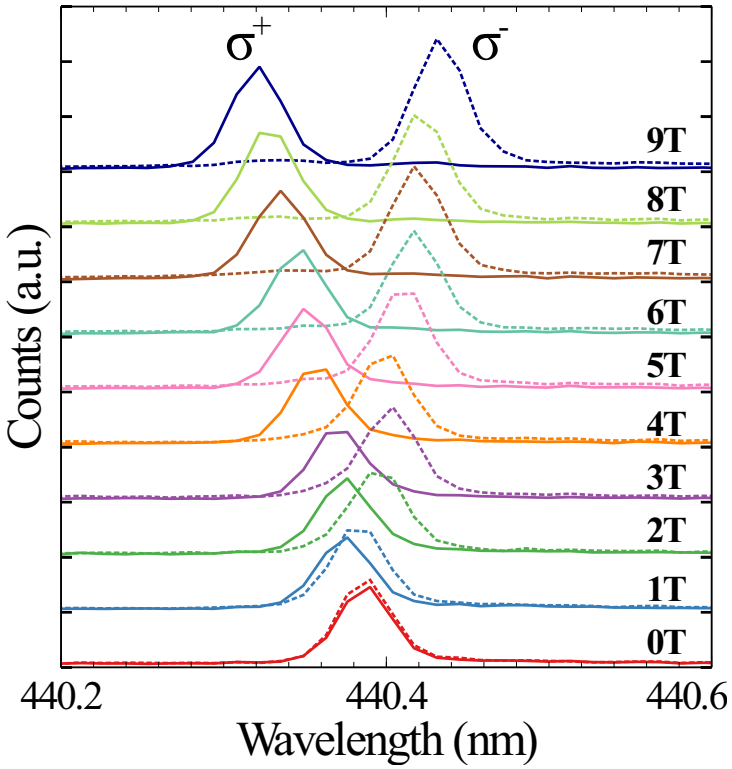

Figure 5.7: Polarization resolved photoluminescence spectrum recorded at increasing magnetic field intensity, showing the splitting of orthogonal circular polarizations.

splitting between those two transitions, we infer $g_{eff} = 0.9$ which is in good agreement with previous results obtained from single fluorine donors in ZnSe. Additionally, we observe a diamagnetic shift of the D^0X emission of $3.25\mu eV/T^2$.

Nonexistence of fine structure splitting and clear splitting into orthogonal circular polarizations are consistent with the expected Kramer's degeneracy of the neutral donor state containing a single electron in its ground state [60].

5.3.3 Voigt Magnetic Field

The optically allowed transitions in this configuration are presented in Figure 5.5. In Voigt configuration four radiative transitions with linear polarization are allowed, two pairs with horizontal (H) and vertical (V) polarization. These four transitions generate two double-connected systems which allow for optical rotation of the electron spin bound to the neutral chlorine donor. The vertically polarized photons can be distinguished from the horizontally polarized photons by using a half-wave plate with the fast axis at an angle of 45°.

5.4 Summary

In this chapter, we first established the presence of the bound donor electron by observing the signature two-electron-satellite emission. Then, we discussed the interaction of the magnetic field with spin states of Cl bound exciton. From the obtained magneto-PL spectra, we experimentally verified the optical selection rules, and inferred the electron and hole g-factors in Faraday configuration. We confirmed the presence of doubly connected lambda system, which allows optical access to different spin states. Our results establish that Cl-bound electron can serve as optically accessible spin qubit with bright excitonic single photon emission.

Chapter 6: Cascaded Single Photon Emission from Biexcitons

In addition to single excitons bound to Chlorine donors, we also identified a different set of narrow lines (exhibited themselves as paired lines) with distinct spectral properties in the sample. With the help of detailed measurements such as power dependent saturation and polarization resolved spetroscopy, we conclude that paired lines can be attributed to biexciton complexes bound to donors in the quantum well.

In this chapter[1], we will discuss the radiative properties of the observed biexcitons. In Section 6.1, we will first discuss the properties of biexcitons and how they can be employed to generate cascaded single photon emission. In Section 6.2, we will share the experimental setup and discuss the techniques that we use to characterize the biexciton emission. In 6.3, we will start with the discussion of PL characteristics. Then, we will use the time resolved PL spectroscopy and statistical correlations between observed pair of lines to prove the existence of cascaded single photon emission. Photon correlation measurements will prove that observed emission is indeed in the form of cascaded single photon emission. Finally, in Section 6.4, we will discuss the polarization of the emission and energy levels of the biexciton state.

[1]The results discussed here will be based on the arXiv:2203.06280

6.1 Radiative Cascades from Biexcitonic Decay

Radiative cascades can be defined as time-ordered emission of photons. If the emitted pairs of photons exhibit single photon statistics, they can be used as on demand sources of entangled photons. One way of realization of cascaded emission in semiconductors is using exciton-biexciton emission pair, where the biexciton consists of two excitons that form a lower energy complex due to Coulombic interactions [64]. The decay of the first exciton initiates a radiative cascade in which the photon emitted by the second exciton may be entangled in polarization [65, 66], time [67], or both [68]. The photon pairs generated through biexciton decay could be used as sources of entangled light with applications in quantum communication [69, 70], photonic quantum computing [71], and quantum metrology [72].

Entangled on demand photon generation from biexcitons are actively being studied in various material platforms including III-V quantum dots [73] and in 2D materials [74]. Impurity atoms in semiconductors are another material platform that shows promise for realizing both sources of quantum light and spin-photon interfaces [15]. Although evidence for biexciton formation has been observed in these materials from isoelectronic impurity dyads [75] and other impurity centers [76, 77], cascaded emission has yet to be demonstrated.

6.2 Experiment Setup

The observation of biexcitons depends on the position on the sample. The most clear feature of them was the pair of lines (mostly separated by 3 nm), which showed equal fine structure splitting. We used the same experimental setup for initial photoluminescence measurements, that we have discussed in the bound excitons Chapter 4. To perform polarization-resolved spectroscopy on the narrow emission lines, we fix the excitation polarization with a linear polarizer with an extinction ratio of 1:106. Photoluminescence signal is filtered from the excitation laser with a notch filter and is passed through a polarization analyzer consisting of a quarter–wave plate, half–wave plate,and linear polarizer. Changing the waveplate angles allowed us to investigate the complex polarization behavior.

One important modification was required to measure the photon correlations between pairs of observed emission lines. Our initial setup was designed to measure auto-correlations of each line, hence a single monochromator (SP-2750, Princeton Instruments) was sufficient to filter the signal. In the new configuration, we introduced a 50:50 beamsplitter before the monochromator, and employed an additional identical monochromator. Using two monochromators allowed us performing narrow filtering at two different wavelengths of interest. We placed identical single photon detectors (PDM Detector, Micro Photon Devices) after each monochromator's exit slit, and measured the time correlations between two detector detections by using time correlated single photon counting module (Picoharp 300). The Figure 6.1 shows the sketch of the experimental setup.

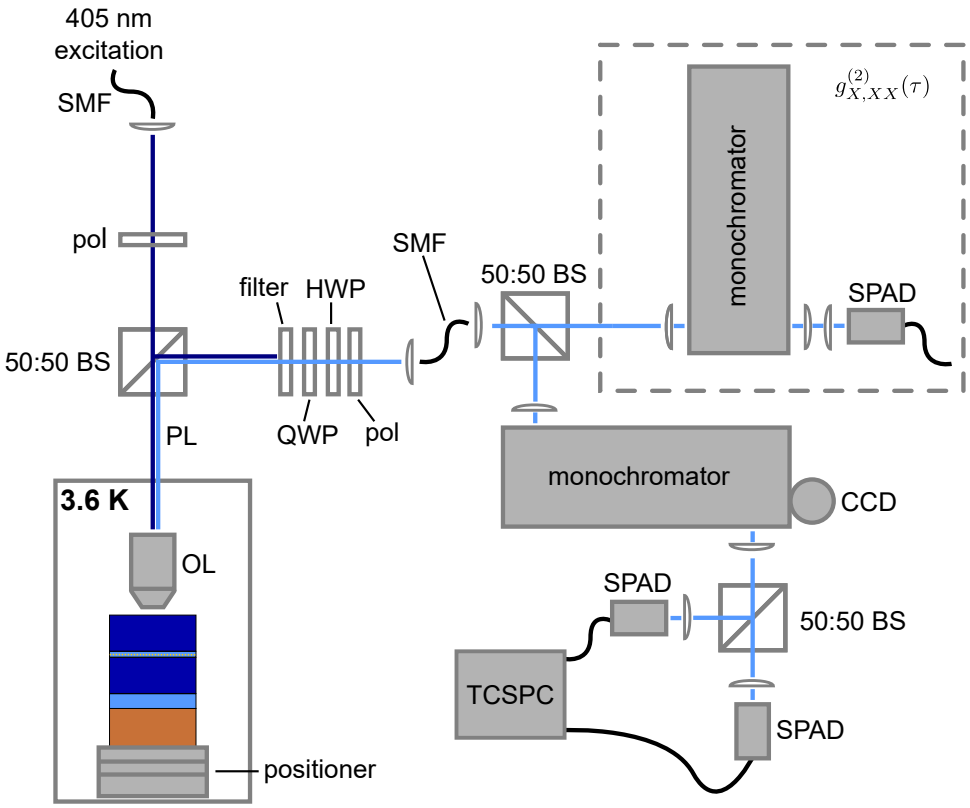

Figure 6.1: Schematic of the optical setup used to investigate optical properties of exciton-biexciton complexes.

6.3 Demonstration of Cascaded Single Photon Emission

In this section, we will present a set of measurements that demonstrates cascaded single photon emission from exciton-biexciton pairs. The first indicator of biexcitonic behavior is coming from photoluminescence measurements. We observe clear emission line-pairs that exhibit a power dependence consistent with an exciton-biexciton cascade. To further reveal the cascading, we use time-resolved decay of the emission performed at low powers, where we only observe single excitons, and high powers where we observe both emission lines. Comparison of two reveals that due to decay of biexcitons, main exciton line is delayed by the lifetime of biexciton decay. Along with lifetime data, photon correlation measurements conclusively reveal the time-ordered nature of the cascade.

6.3.1 Characteristics of PL Response

Using the continuous wave optical excitation above the barrier bandgap at 3.06 eV (405 nm), we efficiently excited the excitons in the quantum well. We show the photoluminescence spectrum from the sample at 3.6 K in Figure 6.2. The highest energy line labeled as FX is due to heavy hole free exciton as discussed in the previous chapter. In addition, we observe a discrete pair of lines $\mathrm{D}^{*}_{\mathrm{A}}\mathrm{X}$ and $\mathrm{D}^{*}_{\mathrm{A}}\mathrm{XX}$ at lower energies. We also observe a second pair of lines visible in the spectrum, $\mathrm{D}^{*}_{\mathrm{B}}\mathrm{X}$ and $\mathrm{D}^{*}_{\mathrm{B}}\mathrm{XX}$, which we attribute to exciton-biexciton emission from a separate impurity center.

Figure 6.3.a shows the excitation power dependence of the emission intensity of the $\mathrm{D}^{*}_{\mathrm{A}}\mathrm{X}$ and $\mathrm{D}^{*}_{\mathrm{A}}\mathrm{XX}$ lines. Although both lines show similar linewidths, we observe markedly different behaviors for each line under increasing excitation power. In the low

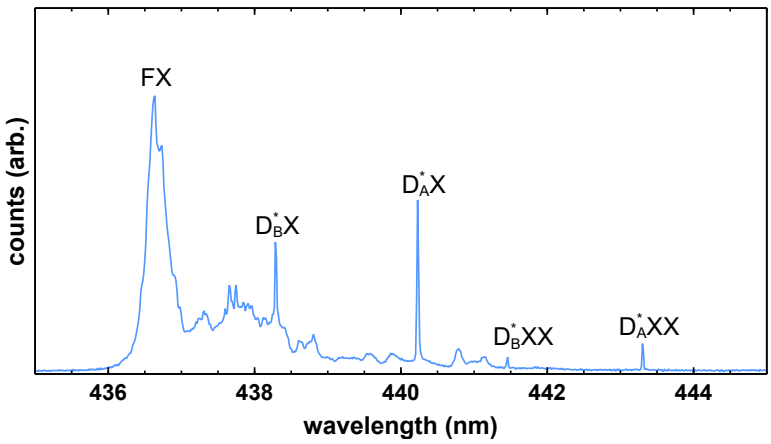

Figure 6.2: Photoluminescence spectrum measured with above band continous wave laser excitation, showing free exciton (FX), bound exciton ($D^*_A X$, $D^*_B X$) and biexciton ($D^*_A XX$, $D^*_B XX$) states

excitation power regime we fit the intensity of each line to $I(p) \propto p^k$, where k is a fit parameter. For the $D^*_A X$ line we observe the exponent $k = 0.95$, indicating nearly linear dependence of the emission intensity on the excitation power. On the other hand, for the $D^*_A XX$ line we observe $k = 1.40$, indicating a super–linear dependence on the excitation power. The nearly linear power dependence of the $D^*_A X$ line and the superlinear power dependence of the $D^*_A XX$ line, followed by saturation of the emission intensity at higher excitation powers, are characteristic of localized exciton and biexciton emission pairs [78].

We also investigate power law behavior of the emission intensity for the $D^*_B X$ and $D^*_B XX$ lines, such that $I(p) \propto p^k$. For the $D^*_B X$ line we observed the exponent $k = 1.09$, while for the $D^*_B XX$ line we observed $k = 1.36$ in the low excitation power regime.

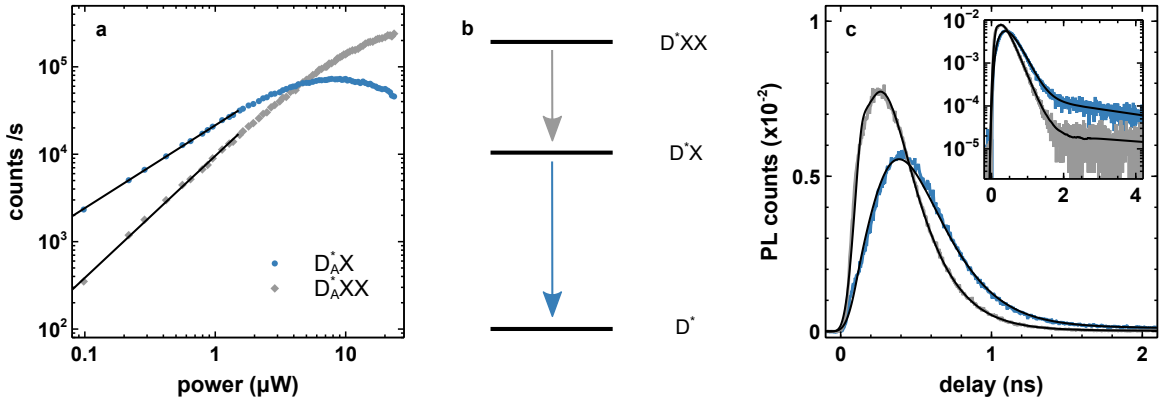

Figure 6.3: a) Power dependent intensity for exciton and biexciton lines b) Energy levels showing exciton and biexciton states c) Time resolved PL intensity showing delayed emission from exciton lines in the presence of biexcitonic emission.

Observing the similar power law trend for both D_A^*X, D_A^*XX and D_B^*X, D_B^*XX lines support the assignment of each line as a localized exciton and biexciton, respectively.

6.3.2 Time Resolved Spectroscopy Results

Figure 6.3.b shows the expected energy level diagram of the biexciton, exciton and ground states. As decay paths reveal, the cascaded emission is originated in the case of biexciton emission. To demonstrate that emission from D_A^*X and D_A^*XX are cascaded, we perform time–resolved lifetime measurements of each line in the emission pair. We excite the sample with 3 ps optical pulses with a photon energy of 3.06 eV from a frequency doubled Ti:Sapphire laser and filter the emission with a grating monochromator. Figure

6.3.c shows the time–resolved measurements of the optical emission from the $D^*_A X$ and $D^*_A XX$ lines. In all panels the recorded transients are normalized by the total number of recorded counts to better show the relative shape of each decay. The solid lines are fits to the data using a multiexponential function convolved with the detector response.

Emission from the $D^*_A XX$ line shows a biexponential decay. By fitting a biexponential decay, we observe a fast time constant of $\tau_1^{XX} = 106$ ps first and a small contribution from a slower time constant of $\tau_2^{XX} = 4.6$ ns second. Emission from the $D^*_A X$ line rises more slowly and reaches its peak intensity only after the onset of $D^*_A XX$ decay. The delay between peak emission of the $D^*_A XX$ and $D^*_A X$ lines is $\sim$ 110 ps, comparable to τ_1^{XX}, suggesting that the decay of $D^*_A XX$ feeds into the $D^*_A X$ state. The decay of the $D^*_A X$ line also exhibits a biexponenial decay with a fast time consant of $\tau_1^{X} = 142$ ps and a slower time constant of $\tau_2^{X} = 3.5$ ns. The slow decay components, τ_2, present in both $D^*_A X$ and $D^*_A XX$ emission may indicate the influence of deeper trapping states, dark excitons, or possible carrier recapture from the quantum well.

To further reveal the time correlations between lines, we monitored each doublet for signs of spectral wandering over a period of 10 minutes. In Figure 6.4, we show the slow drift of the mean emission energy of the $D^*_A X$ and $D^*_A XX$ doublets, and the $D^*_B X$ and $D^*_B XX$ doublets respectively. The D^*_A family of lines show nearly identical behavior, consistent with the picture proposed in the main text of cascaded emission between a localized biexciton and exciton. The D^*_B family of lines also show nearly identical behavior, though we note that the spectral wandering of the D^*_B lines are qualitatively distinct from the D^*_A lines. This difference suggests that $D^*_B X$ and $D^*_B XX$ are localized at a separate impurity complex from D^*_A.

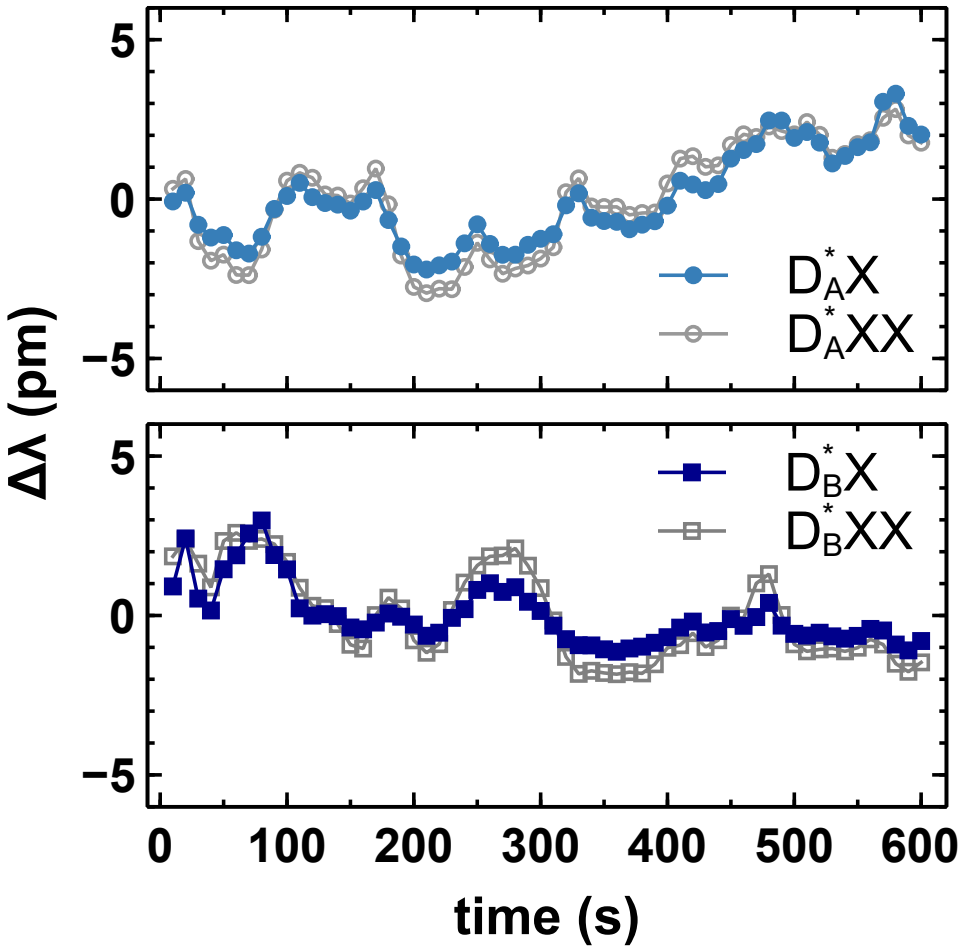

Figure 6.4: PL intensity recorded for 10 minutes showing spectral wandering and intensity correlations between exciton-biexciton lines, for A (top) and B lines (bottom).

6.3.3 Photon Correlation Measurements

More definitive proof of cascaded single emission comes from the study of photon statistics. To demonstrate that each line of emission is due to single photon emission, we measured second order auto-correlation from each emission line in the Hanbury Brown and Twiss configuration. We excited the emitters with 4 picosecond pulse laser at 405 nm with a repetition rate of 76 MHz. Then, after the spectral filtering, we recorded the auto-correlations of both exciton and biexciton line for over 40 hrs. Top and bottom panel of Figure 6.5.a show the second–order autocorrelations of the $D^*_A X$ and $D^*_A XX$ lines respectively. Each correlation is showing photon anti-bunching, given by $g^{(2)}(0) < 0.5$, which verifies the single photon nature of the emitted light. For $D^*_A X$ we measured $g^{(2)}_X(0) = 0.38$, while for $D^*_A XX$ we measured $g^{(2)}_{XX}(0) = 0.43$.

In order to verify the correlations between the cascaded single photons, we perform cross-correlation measurements between the $D^*_A XX$ and $D^*_A X$ emission lines. We used the modified setup, shown in Figure 6.1, with two identical monochromators as spectral filtering devices. We used the pulse excitation (same as auto-correlation measurements), and recorded the counts from each emission line in a separate detector for a time period of 48 hrs. During the long integration, we kept the samples under dark, and ensured the stability of the measurement apparatus by carefully monitoring the counts in detectors. Figure 6.5.b shows the cross–correlation with pulsed excitation which displays significant photon bunching of $g^{(2)}_{X,XX}(0) = 1.78$. The observation of photon bunching, given by $g^{(2)}_{X,XX}(0) > 1$, establishes the enhanced probability of detecting a single photon from the $D^*_A X$ line after first detecting a single photon from the $D^*_A XX$ line. Photon bunching

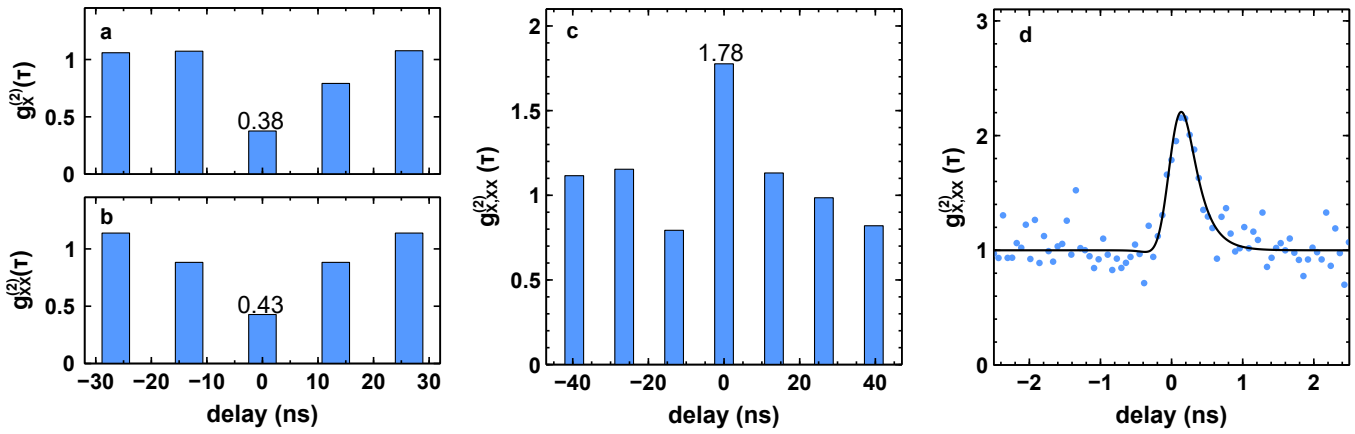

Figure 6.5: Single photon correlation measurements. (a,b) Autocorrelation measurements of (a) the localized exciton line, $g_X^{(2)}(\tau)$, and (b) the localized biexciton line, $g_{XX}^{(2)}(\tau)$. (c,d) Cross–correlation measurements between the localized exciton and biexciton lines, $g_{X,XX}^{(2)}(\tau)$, with (c) pulsed excitation and (d) continuous wave excitation above the quantum well barrier.

provides conclusive evidence for the cascaded relationship between the two emission lines and is therefore direct evidence for the presence of the localized biexciton initiating a radiative cascade.

Measuring the cross-correlation with continuous wave excitation reveals more information about the time dynamics of the cascade. Therefore, we also measured the cross-correlations by using a CW excitation. We used 405 nm CW diode laser (Thorlabs) and the same experimental setup. We recorded the coincidence counts with a time-correlated single photon counting module (Picoharp 300, Picoquant) for a time period of 42 hrs. Figure 6.5.d, reveals characteristic temporal asymmetry of $g^{(2)}_{X,XX}(\tau)$ expected near $\tau = 0$ for cascaded emission [79]. The asymmetry is a signature of $g^{(2)}_{X,XX}(\tau)$ sharply transitioning between antibunching for $\tau < 0$ and bunching for $\tau > 0$. Antibunching arises in the continuous wave measurement because detection of a photon from the $\mathrm{D^*_A X}$ state projects the system into the impurity ground state, out of which a biexciton photon cannot be emitted. The temporal response of our correlation experiment (~ 145 ps) prevented the direct observation of antibunching for $\tau < 0$ at the required time scale, but still allowed the clear observation of the resulting asymmetry of the bunching profile. The fit function is a solution to a three–level rate equation model taking into account the experimentally measured lifetimes of the $\mathrm{D^*_A X}$ and $\mathrm{D^*_A XX}$ states convolved with the measurement system response [79].

6.4 Fine Structure Splitting and Polarization Response

We consistently observe a fine structure splitting from both exciton and biexciton lines. In this section, we will study the polarization characteristics of the fine structure to reveal more insight about the energy level structure of the exciton-biexciton pairs. First observation is that each doublet composed of orthogonal elliptical polarizations. Figure 6.6.a shows polarization resolved spectra of each line. The spectra reveal a fine structure splitting between the orthogonal elliptical components of $\sim \pm 290\ \mu\mathrm{eV}$ for the $\mathrm{D}^*_\mathrm{A}\mathrm{X}$ and $\mathrm{D}^*_\mathrm{A}\mathrm{XX}$ lines, respectively. The equal magnitude but opposite sign of the fine structure splitting suggests that the splitting originates in the localized exciton state $\mathrm{D}^*_\mathrm{A}\mathrm{X}$ [80].

A more detailed polarization analysis is performed to quantify the ellipticity of the emission from of each fine structure component. We perform the polarization analysis using a combination of a quarter-wave plate, half-wave plate, and linear polarizer. Changing the angle of waveplates and recording the modulated PL intensity allowed us to access the relative polarization state of each line. Figure 6.6.b shows the modulated intensities for various angle configurations. We characterize the ellipticity of each line based on the fits in Figure 6.6.b

We model the emitted photoluminescence electric field with an arbitrary polarization in the plane as

$$\mathbf{E}_{\mathrm{PL}} = \begin{pmatrix} E_{0,x} \\ E_{0,y}e^{i\Delta\phi} \end{pmatrix}, \tag{6.1}$$

where $E_{0,x}$ and $E_{0,y}$ are the normalized amplitudes of field along the horizontal and

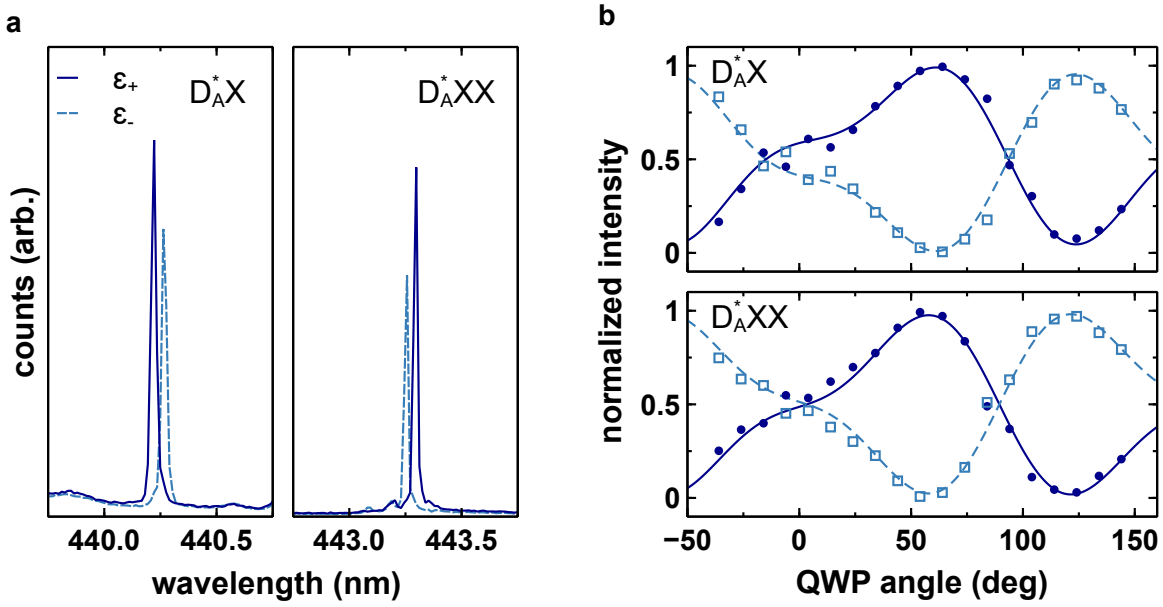

Figure 6.6: Polarization resolved spectroscopy. (a) Measured polarized fine structure of the $\mathrm{D}_{\mathrm{A}}^{*}\mathrm{X}$ and $\mathrm{D}_{\mathrm{A}}^{*}\mathrm{XX}$ lines. (b) Polarization analysis of the $\mathrm{D}_{\mathrm{A}}^{*}\mathrm{X}$ and $\mathrm{D}_{\mathrm{A}}^{*}\mathrm{XX}$ fine structure as a funciton of quarter wave plate angle.

vertical directions, and $\Delta\phi = \phi_y - \phi_x$ is the relative phase difference between each component. Each optical element can be modeled by a matrix that indicates it's effect on the polarization components of incident light that are either parallel or perpendicular to the element's birefringent axis. For the quarter–wave plate, half–wave plate, and linear polarizer we have respectively,

$$\mathbf{M}_{\mathrm{QWP}} = e^{i\pi/4}\begin{pmatrix} 1 & 0 \\ 0 & -i \end{pmatrix}, \mathbf{M}_{\mathrm{HWP}} = e^{i\pi/2}\begin{pmatrix} 1 & 0 \\ 0 & -1 \end{pmatrix}, \mathbf{M}_{\mathrm{POL}} = \begin{pmatrix} 0 & 0 \\ 0 & 1 \end{pmatrix},$$

where the fast axis of each wave plate and the transmission axis of the polarizer were each taken to be vertical. A rotation of each element by an angle θ can be considered with the rotation matrix

$$\mathbf{R}(\theta) = \begin{pmatrix} \cos\theta & -\sin\theta \\ \sin\theta & \cos\theta \end{pmatrix}, \tag{6.2}$$

such that $\mathbf{M}(\theta) = \mathbf{R}(\theta)^{-1}\mathbf{M}\mathbf{R}(\theta)$. The transmission intensity of the photoluminescence signal through the polarization analyzer can then be described by

$$|\mathbf{E}_{\mathrm{t}}|^2 = |\mathbf{M}_{\mathrm{POL}}(\theta_p)\mathbf{M}_{\mathrm{HWP}}(\theta_h)\mathbf{M}_{\mathrm{QWP}}(\theta_q)\mathbf{E}_{\mathrm{PL}}|^2, \tag{6.3}$$

where θ_p, θ_h, and θ_q are the rotation angles of the polarizer, half–wave plate, and quarter–wave plate respectively. In the experiment described in the main text, the transmission axis of the polarizer is taken to be vertical and the fast axis of the half–wave plate is

aligned to the polarizer, such that $\theta_p = \theta_h = 0$. Therefore, the transmission intensity of the polarization analyzer is given as

$$|\mathbf{E}_\mathrm{t}|^2 = \frac{1}{2}|e^{i\Delta\phi}E_{0,y}(1 - i\cos 2\theta_q) + iE_{0,x}\sin 2\theta_q|^2. \tag{6.4}$$

In the experiment, the transmission intensity is monitored as the quarter–wave plate angle is rotated. The data is then fit to Equation 6.4, taking $E_{0,x}$ and $\Delta\phi$ as fit parameters and restricting $E_{0,y}$ by the normalization condition to determine the polarization of the emitted photoluminescence.

The Stokes parameters of the signal can be directly determined using the extracted values of the amplitudes and relative phase for the components of $\mathbf{E}_\mathrm{PL}$ by then calculating

$$\begin{aligned}
s_0 &= \mathrm{E}_\mathrm{PL}^{(\mathrm{x})}\mathrm{E}_\mathrm{PL}^{(\mathrm{x})^*} + \mathrm{E}_\mathrm{PL}^{(\mathrm{y})}\mathrm{E}_\mathrm{PL}^{(\mathrm{y})^*} \\
s_1 &= \mathrm{E}_\mathrm{PL}^{(\mathrm{x})}\mathrm{E}_\mathrm{PL}^{(\mathrm{x})^*} - \mathrm{E}_\mathrm{PL}^{(\mathrm{y})}\mathrm{E}_\mathrm{PL}^{(\mathrm{y})^*} \\
s_2 &= \mathrm{E}_\mathrm{PL}^{(\mathrm{x})}\mathrm{E}_\mathrm{PL}^{(\mathrm{y})^*} + \mathrm{E}_\mathrm{PL}^{(\mathrm{y})}\mathrm{E}_\mathrm{PL}^{(\mathrm{x})^*} \\
s_3 &= i\left(\mathrm{E}_\mathrm{PL}^{(\mathrm{x})}\mathrm{E}_\mathrm{PL}^{(\mathrm{y})^*} - \mathrm{E}_\mathrm{PL}^{(\mathrm{y})}\mathrm{E}_\mathrm{PL}^{(\mathrm{x})^*}\right),
\end{aligned}$$

where s_0 gives the total intensity, s_1 determines the prevelance of vertical and horizontal components of the total intensity, s_2 determines the prevelance of diagonal and anti–diagonal components, and s_3 determines the prevelance of right and left handed circular components. From each fit we determined the ellipticity angle χ, defined in terms of the polarization ellipse as $\tan\chi = \varepsilon$, where ε is the ratio between the ellipse's minor and

major axes. In terms of the calculated Stokes parameters, the angle χ can be expressed as $\sin 2\chi = s_3/s_0$.

The angle χ therefore assumes the value $\chi = 0$ $(\pm\pi/4)$ for linear ($\sigma_\pm$ circular) polarizations. For the $\mathrm{D}^*_\mathrm{A}\mathrm{X}$ doublet we found $\chi_{p_1,p_2} = \mp 0.13\pi$, while for the $\mathrm{D}^*_\mathrm{A}\mathrm{XX}$ doublet we found $\chi_{p_1,p_2} = \mp 0.14\pi$ in close similarity.

The ellipticity of the fine structure components observed here contrasts with typical observations of neutral biexciton cascades in self–assembled quantum dots where the fine structure components are well described by orthogonal linear polarizations [65]. The magnitude of the fine structure splitting and optical polarization of each line are closely related to the confinement symmetry and charge configuration of the localized excitons, and typically emerges from a confinement symmetry below D_{2d} [80]. Possible candidates for the observed impurity center are a neutral chlorine donor (D^0), an ionized Chlorine donor (D^+), which is stable in ZnSe and known to have a higher excitonic binding energy than the neutral donor [43], or potential multi–donor complexes which cannot be ruled out. In particular, the observed elliptical polarization of the fine structure components may be explained by anisotropic electron–hole exchange in the presence of a highly charged biexciton cascade [81, 82]. Further understanding of the impurity center's charge configuration will enable strategies for minimizing the observed fine structure splitting, which is a requirement for realizing a source of entangled photons. Strategies for minimizing the fine structure splitting may include tuning with electric or magnetic fields or strain [83–85].

6.5 Summary

In this chapter, we reported the observation of biexcitons in a chlorine doped ZnSe quantum well. The power dependent intensity measurements showed that excitons and biexcitons exhibited linear and superlinear power dependence, respectively. We confirmed the single photon nature of both exciton and biexciton line by measuring the second order auto correlation measurements in Hanbury Brown and Twiss configuration. The resulting radiative cascade was clearly observed in both time–resolved photoluminescence and single–photon correlation measurements. The observed fast decay times of 106 ps and 142 ps for the biexciton and exciton further highlight the promise of this system to produce fast and bright emission of single photons and photon pairs. These results provide a path for the development of on–demand sources of entangled photons with impurity atoms in semiconductors.

Chapter 7: Design and Fabrication of Nanophotonic Cavities

7.1 Introduction

Photonic crystals (PCs) are devices that have periodically modulated refractive index. The local refractive index changes can be achieved with various techniques such as removing the material (making holes), doping and placing a different materials periodically [86].

The propagation of electromagnetic waves in a medium obeys certain phase relations. The modulation of refractive index by introducing periodic elements in the length scales of optical wavelengths can lead to suppression of certain modes while supporting the others. Changing the local refractive indexes and periodicity allows engineering photonic crystals to open a photonic band gap, which prohibits the propagation of photons for certain directions within some frequency range [87].

Introducing local defects in a photonic crystal can lead to lateral confinement of electromagnetic mode in the defect site in the photonic band gap. The out-of-plane confinement is achieved by using thin slab of material suspended in the air. The total internal reflection provides the out-of-plane confinement, hence 3D confinement of the mode is achieved. Such devices are called photonic crystal cavities due to their highly localized, cavity-like, mode distributions. The optical properties of defect modes can be

engineered by tailoring the geometrical parameters of defect site such as size , shape and type of defects. Hence, designing photonic crystal with defects allows controlling the mode profile, resonant frequency, mode volume and quality factors [88].

Integration of photonic crystal cavities with quantum emitters serves multiple purposes. First, the coupling of quantum emitter radiation to cavity modes can lead to increase of the brightness of emitter via the Purcell effect [89]. Secondly, it allows engineering the radiation pattern of the emission to increase the directionality of emission [90]. Due to coupling of emitter to the cavity mode, the far field radiation pattern is governed by the field distribution of the cavity which can be engineered by tailoring the defect parameters. One greater application is to exploit the cavity quantum electrodynamics. When the emitter is strongly coupled to the cavity mode, the reflectivity of the cavity can be modulated by the existence of excited state coupled to the cavity resonance [91]. This can lead to realization of quantum gates with single qubits [92].

Photonic crystal cavities integrated with quantum emitters have been demonstrated in various semiconductor platforms. Here, we will focus our attention to design,fabrication and testing of a spesific photonic crystal cavity in ZnSe designed to operate at wavelengths of bound exciton emission. Here, we limit our interest only to showing a proof of concept device that can work in ZnSe. Hence, our results are far from being comprehensive, but establishes that photonic structures can be designed and manufactured in ZnSe for future integration of quantum emitters.

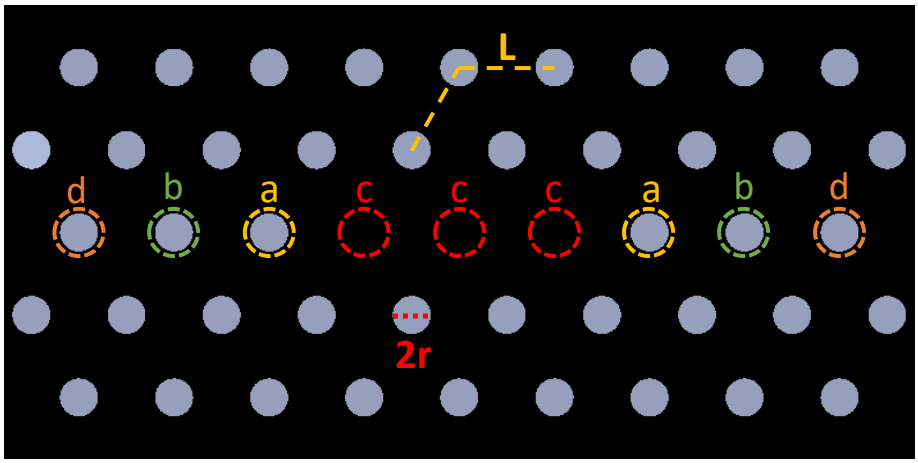

Figure 7.1: Schematic of L3 cavity. Three missing holes as linear line at the center, labeled as c, forms the cavity in the triangular lattice. The geometrical parameters optimized for the design has been labeled as lattice constant (L), radius (r), displacements (a,b,d).

7.2 Design of L3 Photonic Crystal Cavities

The starting photonics crystal consists of a slab of material with etched holes in the form of triangular lattice. Removing the three holes at the center allows the confinement of the mode, and forms the basis for the L3 cavity [93]. The Figure 7.1 shows the schematic of the cavity design, where missing holes are represented by dashed circles, labeled c. The quality factor of the resonance can be increased by decreasing the radiation losses. This can be achieved varying the size of the etched holes nearby the cavity and by displacing the end holes in the outward direction.

The cavity supports multiple modes. The fundamental mode (called as M1) has longest wavelength and highest quality factor. The wavelengths of resonances depend on the lattice constant (labeled as L). Hence, changing the periodicity of holes allows matching the resonance wavelength to bound exciton emission wavelength, 440 nm.

We performed FDTD simulations by using a commercial simulation package (ANSYS Lumerical) to find the physical parameters of the design. The thickness of suspended ZnSe slab is set to 100 nm. Changing the parameters namely lattice constant (L), hole radius (r) and displacement of nearby holes (a,b,d), we optimized the quality factor at the wavelength of interest.

In the first design, Q factor of $50,000$ has been achieved by setting the $L = 134\ nm$, $r = 27\ nm$, $a = 33\ nm$. The Figure 7.2.a shows the electric field intensity of the M1 mode at resonance. The cavity mode is confined in the region where the missing holes are located. The field intensity decreases rapidly in the lateral direction since no modes are supported to the photonic band gap. Although this design achieves very high quality factors, there are two issues. First, the far field radiation pattern (shown in Figure 7.2.b) exhibits two strong lobes at high angles. Due to limited numerical aperture of the optical setup, this mode is hard to collect with the objective lens, hence it is not feasible in terms of measurement perspective. The another issue is the physical sizes of holes and displacements. The numbers mentioned above are already in the limit of our fabrication resolution, hence this design is hard to fabricate robustly even by using state-of-art nanofabrication techniques.

To address both issues, we re-designed the cavity by sacrificing from quality factors. In the new design, we achieved Q-factor of $35,000$ by setting $L = 134\ nm$, $r = 38\ nm$,

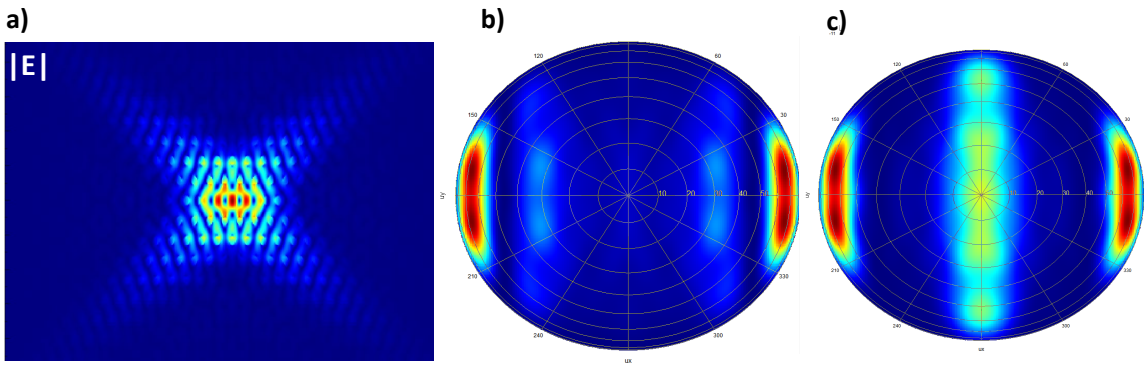

Figure 7.2: FDTD simulation results. a) Electric field intensity distribution of the fundamental mode at the resonance b) Far field radiation pattern of high-Q design c) Far field radiation pattern of lower-Q design

$a = 27\ nm$ and $d = 27\ nm$. The far field pattern of the new design shows that increased ratio of the emitted radiation is within the acceptance cone of our objective. Therefore, we have chosen to proceed with these parameters.

7.3 Fabrication of Cavities

The sample is composed of $100\ nm$ thick $ZnSe/ZnMgSe$ quantum well layer epitaxially grown on $GaAs$ substrate. The details of the quantum well and sample growth have been discussed in the Chapter 3. The Figure 7.3 depicts the steps of fabrication recipe.

To fabricate the photonic crystal cavities, we used high resolution e-beam lithography with directional etching. We discuss the detailed steps below.

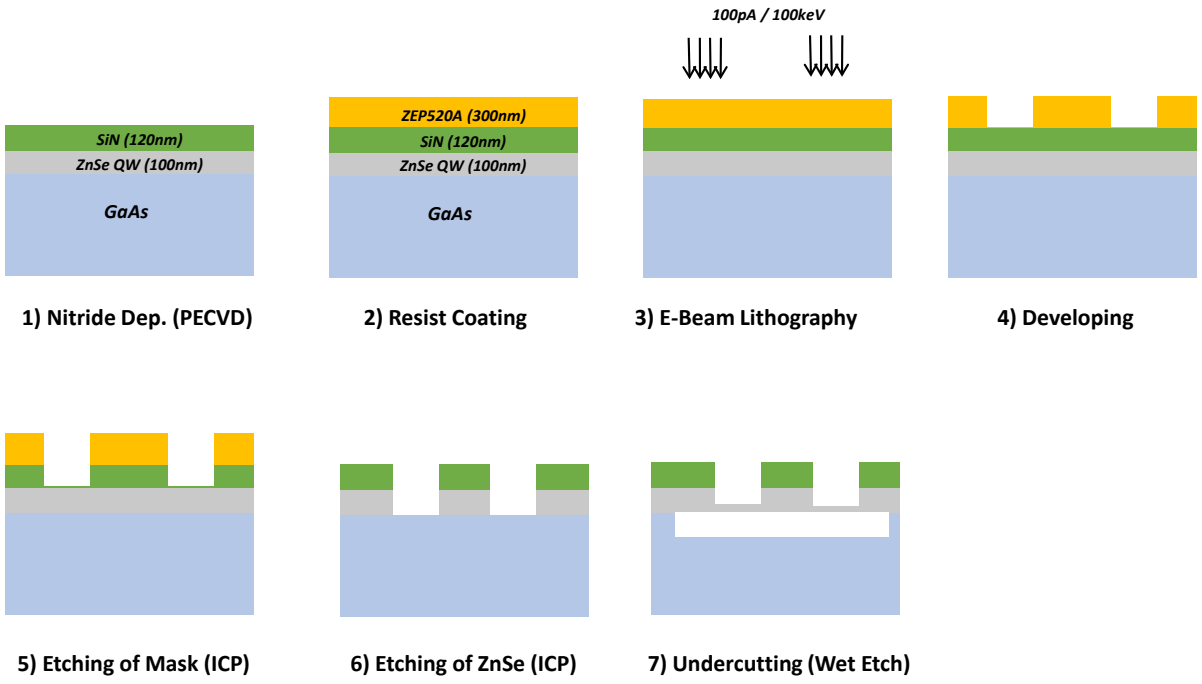

Figure 7.3: Nanofabrication steps to create suspended photonic crystal cavities

In the first step, we deposited $120\ nm$ SiN by using Plasma Enhanced Chemical Vapor Deposition (PECVD). The thin SiN layer serves as hard mask while etching the ZnSe. The thickness of SiN has been determined by measuring the etch rates ZnSe and selectivity of recipe between ZnSe and SiN.

Secondly, we spin-coated a positive e-beam resist (ZEP520A) diluted with a solvent (Anisole). The diluting the resist and using high spin coating speeds (4000 rpm) allowed us achieving very thin layer of resist (160 nm) to achieve the better resolution needed for small holes.

Then, we performed electron beam lithography (Elionix ELS-G100) by using 100 pA current with 100keV acceleration energy. The small radius of holes requires very high resolution, therefore very careful alignment of the beam is necessary to achieve the increased resolution. The exposed regions of resist is then developed by using developers MIBK and ZED.

The directional etching is composed of two steps. In the first step, we transferred the resist pattern to the SiN mask layer by using F based Inductively Coupled Plasma Etching (Oxford ICP-RIE). Then, we used another recipe optimized for directional etching of ZnSe to transfer the mask pattern to the ZnSe layer.

To make ZnSe slab suspended, we used a wet chemical etch step to selectively etch GaAs underneath. To allow the etchant to reach underneath uniformly, we placed large rectangular holes around the PC. Considering the small size of etched holes, it is critical to have very selective wet etch, etching GaAs while not etching the ZnSe layer.

The Figure 7.4 shows SEM images of the fabricated device after all steps. Using a wet etch recipe that is not perfectly selective results in enlarged holes. Our wet etch

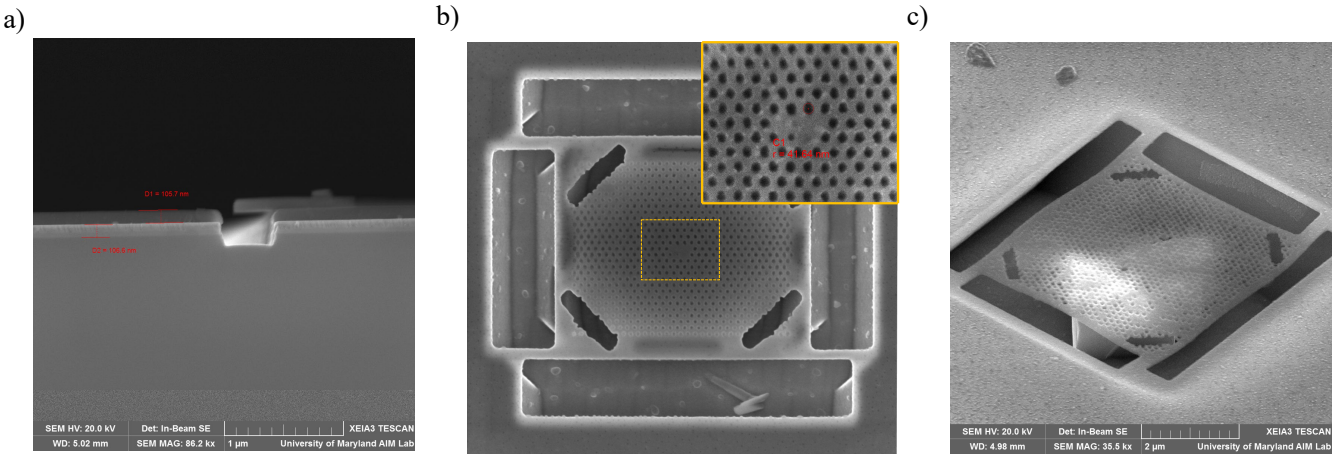

Figure 7.4: SEM images of fabricated photonic crystal cavities. a) Cross sectional view of the etched lines, showing the directionality of the dry etch process. b) Top view showing the triangular lattice with 3 missing holes, forming L3 cavity. Inset shows the close up image of the cavity region. Rectangular holes around the structure are etched to facilitate undercutting of GaAs to make structures suspended. c) Angled view image of the fabricated device, showing that substrate is not etched completely.

recipe did not have perfect selectivity, therefore we had to limit etching time not to distort holes more than tolerable limits. That resulted in partial etching of the substrate material, as seen in the Figure 7.4.c.

To address the undercut issue, we recommend using a modified layer structure as shown in Figure 7.5. Using a sacrificial layer such as AlGaAs will allow us using more selective chemical such as HF, and hence will result in better undercut while maintaining the size and shape of the etched holes. Nonetheless, we will discuss the measurement results of only the original structure in the next section. We leave the rest as an open question to the future fellow researchers.

7.4 Optical Characterization

To measure cavity properties, we mount the sample in a closed-cycle cryostat and we kept the sample at 3.6K. We excite the sample with 405 nm CW laser, that excites both free excitons and bound excitons. We collect this emission with a confocal microscope with an objective lens, NA of 0.7. Even in the absence of narrow lines originated from bound excitons, sample PL shows a faint background in the broader range of wavelengths between (437 nm to 442 nm). We use this background emission to hunt for cavity resonances.

Due to fabrication imperfections and non-perfect modeling of refractive index of ZnSe/ZnMgSe layer, the fabricated structures may deviate from the designed optical optical response. To mitigate those effects, we fabricated various designs with varying geometrical parameters. Then, we scanned the sample and look for signs for cavity

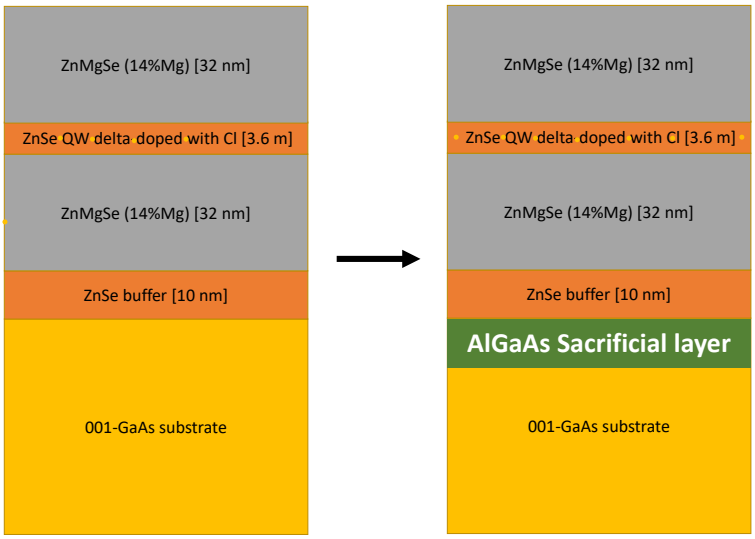

Figure 7.5: Layer structure of the fabricated devices. Left image shows the the sample in-use. Lack of sacrificial layer resulted in non-selective etching of GaAs. Right image shows the proposed structure with AlGaAs sacrificial layer.

resonance.

The Figure 7.6 shows the spectrum of the device with a cavity mode. The blue curve shows the reference spectrum measured at the unstructured portion of the sample. On the photonic crystal structure, the center wavelength of the FX line is slightly red-shifted due to the strain relief, and it is consistent when measured on other devices in the same chip. The enhanced peak at 445, on the other hand, is device dependent and only brightens at the center of the photonic crystal, where the cavity is located. We measure the quality factor of this peak as 110, which is two orders of magnitude smaller than FDTD results. The difference can be explained by non-perfect etching of the substrate. As seen in the Figure 7.4, non-etched substrate creates lossy path towards the high-refractive index substrate, significantly decreases the quality factor of the cavity.

7.5 Discussions

In this chapter, we discussed our attempts to realize photonic crystal cavities on ZnSe platform. Our efforts to achieve high-q cavities coupled to donor bound excitons are interrupted mainly due to non-availability of the material with the sacrificial layer. However, the photonic designs and fabrication results showing patterning of ZnSe establishes that ZnSe photonic cavities can be integrated with donor bound excitons. We worked towards this goal by working with our collaborators who are specializing in the MBE growth. However, those studies will be the topic of another thesis.

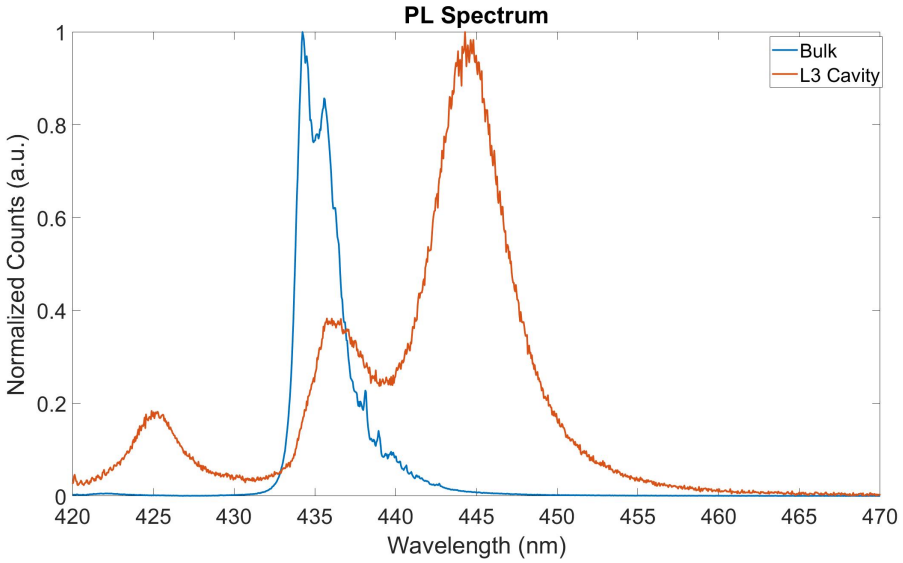

Figure 7.6: The measured spectrum of the sample. Blue line shows PL spectrum from unpatterned bulk region. The orange curves demonstrates cavity mode with q-factor of 110. The low q-factor is caused by radiative losses, due to non-perfect undercutting.

Chapter 8: Conclusion and Outlook

Using solid state qubits to realize scalable quantum computing has a great advantage due to our capabilities to process solid state materials with modern nanofabrication methods. Integrating photonic devices with solid state qubits in the same platform enables realization of efficient spin-photon interfaces to read/write quantum information by using photons. Furthermore, lossless photonic pathways allows the routing of quantum information encoded photons to any place on the chip.

Great benefits of scalability and photonic integration have led to numerous efforts to implement qubits in solid-state systems. Quantum light sources and solid state qubits have been extensively explored for various platform ranging from quantum dots to color centers in diamond. However, we are still lacking a qubit system that provides the full set of capabilities required to achieve scalable quantum technology.

Donor impurities in ZnSe were proposed as the basis for single photon sources and qubits. To this extent, only flourine impurities have been isolated as single impurities to date.

In this thesis we aimed to investigate single Cl impurities in ZnSe for their radiative properties and quantum applications. We achieved the optical isolation of single impurities in the unstructured ZnSe by using low doping concentration samples and high-resolution

confocal spectroscopy.

Donor bound excitons in ZnSe exhibit very small binding energies that leads to short radiative lifetimes and bright emission. However, due to background emission originated from free excitons in the material, high single photon purities are hard to achieve. To increase the binding energies of bound excitons, we employed the quantum confinement effect. We delta doped Cl impurities in the center of ZnSe/ZnMgSe quantum wells. Using the quantum well increased the confinement of bound excitons, resulting in high brightness and high binding energies.

We performed complete characterization of radiative properties of Cl bound excitons in Chapter 4. The photoluminescence measurements showed that Cl bound excitons have narrow linewidths with small inhomogeneous broadening. Time resolved photoluminescence data show that they also exhibit short lifetimes in the order of 200 ps. We confirmed the single photon emission by measuring the second order auto correlations in Hanbury Brown and Twiss configuration. Our study shows that Cl bound excitons are promising single photon sources with high brightness and small inhomogeneity. Future studies may focus on the improvement of single photon emission by integrating emitters with nanophotonic devices such as photonic crystals and bulls-eye cavities. Our first results establish that temperature tuning can be employed at some extent to tune the emission wavelength. The other tuning mechanisms such as strain tuning and Stark shift may also be investigated to increase the tuning capability.

We studied the energy levels of the Cl bound electron in Chapter 5 to investigate the potential for spin-qubit applications. We started with the discussion of energy levels of single electron system and recombination pathways for the excited state. The observation

of two-electron-satellite emission upon resonant excitation established that Cl impurity hosts a single electron in its ground state. After confirming the presence of the ground state electron, we discussed how energy states of neutral donor evolves under the applied magnetic field. Polarization-resolved photoluminescence measurements revealed allowed optical transitions and effective g-factors. Our results establishes that Cl impurity hosts a single ground state electron that can serve as a potential spin qubit. To realize the optical control of the electron spin, in-plane magnetic field may be used in the future studies. In Voigt configuration, optical pumping of desired spin states can be realized and electron spin dephasing times can be characterized. To improve the spin coherence times, spin purification of the host crystal may be performed and dilution fridge temperatures may be exploited.

In Chapter 6, we reported the observations of exciton-biexciton pairs from the same Cl complex. We confirmed the single photon nature of both exciton and biexciton emission lines by measuring the photon statistics. The time resolved photoluminescence data showed short lifetimes from both exciton and biexciton line. Finally, we studied photon emission correlations between exciton and biexciton pairs, proving the cascaded emission. Our results are first time demonstration of cascaded single photon emission from an impurity based system. Demonstration of fast, cascaded single photon emission from Cl complexes provides a path for the development of on–demand sources of entangled photons with impurity atoms in semiconductors.

In Chapter 7, we discussed the design, fabrication and testing of photonic crystal cavities on ZnSe platform. We, first started with FDTD simulation results, discussing the cavity mode and far-field emission pattern. Then, we developed a nanofabrication

recipe to create suspended photonic crystal cavities, and showed images of the devices that we fabricated. The optical characterization showed that cavities exhibit high losses, which limit their quality factors. We identified the source of the loss as etched parts of the substrate, which is caused by non-perfect undercut recipe. To increase the selectivity, we proposed a modification in the MBE growth process. Future studies may involve using sacrificial layers to allow easier undercut of the samples. Moreover, other photonic devices such as bulls-eye cavities or nanobeam cavities may be investigated.

The results presented in this thesis provide a first complete study of single Cl impurities in ZnSe. Promising radiative properties, suitable spin states and potential to integrate emitters with photonic devices demonstrate significant potential of Cl bound excitons. Based on the works presented in this thesis and further potentials to be realized, single Cl impurities in ZnSe manifest themselves as attractive quantum light sources and appealing solid-state based qubit candidate.

Appendix A: Fabrication Details

A.1 Nanofabrication Recipe for ZnSe Photonic Crystals

Step 0: Cleaning

Before starting the fabrication, the sample is cleaned thoroughly. The cleaning steps are as follows:

- *Acetone* [90 seconds]
- *Methanol* [90 seconds]
- *IPA* [90 seconds]
- *DI Water* [90 seconds]
- *Hot Plate* [90 seconds]

Step 1: Silicon Nitride Deposition

120 nm Silicon Nitride (SiN) is deposited with PECVD.

Pressure : 1000 mTorr

Table Heater : 300 °C

Chiller Control: 70 °C

Time: 5 minutes

Conditioning:

Purge with 500 sccm N2 [30 seconds]

Gases:

- $\%5$ SiH_4 $\%95$ N_2 [400 sccm]
- NH_3 [20 sccm]

Powers:

- LF : 30 Watts [7 seconds]
- RF : 20 Watts [13 seconds]

Step 2: Resist Coating

ZEP 520A (5) : Anisole (3) [mass ratio]

4000 rpm, 50 seconds

Thickness: 150 nm

Step 3: E-Beam Lithography

Beam Current: 100 pA

Acceleration: 100 keV

Write Field: 100 μm

Pitch: 80 pm

Dose: 300 $\mu C/cm^2$

Step 4: Etching of Silicon Nitride Mask

Pressure : 10 mTorr

Table Temperature : 5 $^\circ C$

He Backing : 7.5 sccm

Time : 43 seconds [full etch]

Gases:

- CHF_3 [45 sccm]
- SF_6 [5 sccm]

Powers:

- RF : 50 Watts
- ICP : 500 Watts

Step 5: Removal of Resist Residue

Hot PG remover [$\gg$ 2 hrs]

Step 6: Etching of ZnSe

Pressure : 4 mTorr

Table Temperature : 60 °C

He Backing : No

Time : 17 seconds

Gases:

- CHF_3 [45 sccm]
- SF_6 [5 sccm]

Powers:

- RF : 50 Watts

- ICP : 500 Watts

Step 7: Removing Hard Mask

22 seconds of *Step 4*

Step 8: Undercut

Time: 2 minutes

Mixture H_2O_2 [7mL] + H_2O [190mL]+ NaOH [1.72 gram]

Appendix B: Other Research Contributions

B.1 Demonstration of Robust Quantum Photonic Devices with Topological Edge States

In this work (Appendix C: Publication J.3), we use the topological insulator concepts from the condensed matter physics to implement topologically robust edge states at the interface between two topologically distinct photonic crystals. We use finite-difference-time-domain simulation (FDTD) techniques to design two perturbed honeycomb photonic crystals, for which equilateral triangular air holes are shifted concentrically inward and outward direction, respectively. We show that confined edge modes exist at the interface with chiral propagation properties. To show the presence of the guided mode coupled to the embedded quantum emitter, we excite the Gallium Arsenide/Indium Arsenide (GaAs/InAs) quantum dots and measure the transmission at both ends by outcoupling the light via diffraction gratings. To demonstrate the helical light matter coupling, we apply a magnetic field to induce Zeeman splitting, and separate two orthogonal circular polarizations of quantum dot emission. Then, we spectrally resolve the opposite polarizations in opposite ends of the waveguide, which proves the chiral coupling of the emitter. We verify the robustness of the waveguide by implementing various bends on straight waveguide and

measuring the transmission.

By using a similar topological framework, in another work (Appendix C: Publication J.4), we demonstrate a topological resonator that exhibits strong light-matter interactions. In our earlier work, we demonstrate that sharp bends do not cause any significant scattering due to the topological protection. We use this advantage to make sharp bends that form closed loop circuit-track resonator. We use FDTD simulations to determine the length of the resonator to create measurable free spectral range. Then, we fabricate our structures with nanofabrication techniques. We demonstrate a cavity induced Purcell enhancement of 3.4 by measuring the intensity enhancement of the quantum dot. Our novel experimental results open an avenue to design complex nanophotonic circuits for quantum information processing and to study novel quantum many-body dynamics.

In this project, I developed the fabrication process for GaAs and partially contributed the characterization of devices. I employed electron beam lithography and dry etching steps to achieve high-resolution fabrication of photonic crystals. I optimized the e-beam layout to allow realization of sharp triangular features. For the characterization of the samples, I used a home-built optical measurement setup, and performed polarization-resolved photo-luminescence measurements.

B.2 Integration of Quantum Emitters with Telecom Photonics

Quantum networks have great potential applications such as distributed quantum information processing and quantum key distribution. One of the many requirements to realize such networks is to efficiently extract the quantum light from the solid state

systems and to efficiently couple it to the existing telecom photonics infrastructure. In this project, we integrate Indium phosphide/Indium Arsenide (InP/InAs) quantum dots emitting at telecom wavelengths to telecom fiber optics and lithium niobate photonics. We use finite-difference-time-domain methods to design InP nanobeam waveguides with tapering tip to efficiently couple quantum dot emission into much larger waveguide modes such as integrated lithium niobate waveguides and optical fibers. The one end of the waveguide utilizes distributed Bragg gratings to reflect light into the tapered side. By increasing the taper length, we adiabatically change the mode size of the nanobeam and match it to mode size of the corresponding waveguide mode. We fabricate our designs with e-beam lithography and directional plasma etching.

In the first part of the project (Appendix C: Publication J.6), we transfer InP nanobeam waveguides to the another photonic chip by using a technique called as "pick-and-place". In this method, we utilize Tescan FIB/SEM system integrated with a motorized tungsten probe, and remove the suspended nanobeam waveguides from the sample and transfer them to the on top of pre-fabricated lithium niobate waveguides. Due to the evanescent coupling between two waveguide modes, we are able to efficiently extract the quantum dot emission into the lithium niobate waveguides. Then, we outcouple the light from the lithium niobate photonic integrated circuit to characterize the coupling efficiency and to measure photon statistics. In the second part of the project (Appendix C: Publication J.5), we use a similar nanobeam waveguide design to couple light directly to tapered single mode fiber optic cables. Using tapered nanobeam waveguide and tapered fiber tip, we show efficient coupling between the single quantum emitters and the single mode fiber. Our results establish that quantum dots emitting at telecom wavelengths can be integrated

with mature photonic integrated circuits and existing fiber optic networks.

In this project, I designed the nanobeam waveguides with Bragg gratings and developed the fabrication process to create suspended InP devices. I used the FDTD simulation techniques to optimize the waveguide geometry in coordination with other designers. I employed electron beam lithography and dry etching steps to achieve high-resolution fabrication of the suspended nanobeam waveguides. In coordination with the transfer team, I optimized the nanofabrication recipe to increase the yields of the pick-and-place process.

Appendix C: List of Publications and Conference Talks

J.1. **A. Karasahin**, R.M. Pettit, N. von den Driesch, M.M. Jansen, A. Pawlis, E. Waks, "Single quantum emitters with spin ground states based on Cl bound excitons in ZnSe", arXiv:2203.05748, under review.

J.2. R.M. Pettit, **A. Karasahin**, N. von den Driesch, M.M. Jansen, A. Pawlis, E. Waks, "Correlations between cascaded photons from spatially localized biexcitons in ZnSe", arXiv:2203.06280, under review.

J.3. S. Barik, **A. Karasahin**, C. Flower, T. Cai, H. Miyake, W. DeGottardi, M. Hafezi, E. Waks, "A topological quantum optics interface", *Science*, 359, 6376 (2018).

J.4. S. Barik, **A. Karasahin**, S. Mittal, E. Waks, M. Hafezi, "Chiral quantum optics using a topological resonator", *Physical Review B*, 101, 20 (2020).

J.5. C.M. Lee, M.A. Buyukkaya, S. Aghaeimeibodi, **A. Karasahin**, C.J.K. Richardson, E. Waks, "A fiber-integrated nanobeam single photon source emitting at telecom wavelengths", *Applied Physics Letters*, 114, 17 (2019).

J.6. S. Aghaeimeibodi, B. Desiatov, J.H. Kim, C.M. Lee, M.A. Buyukkaya, **A. Karasahin**, C.J.K. Richardson, R.P. Leavitt, M. Lončar, E. Waks, "Integration of quantum dots with lithium niobate photonics", *Applied Physics Letters* 113, 22 (2018).

J.7. Z. Luo, S. Sun, **A. Karasahin**, A.S. Bracker, S.G. Carter, M.K. Yakes, D. Gammon, E. Waks, "A Spin–Photon Interface Using Charge-Tunable Quantum Dots Strongly Coupled to a Cavity", *Nano Letters* 19, 17 (2019).

C.1. **A. Karasahin**, R. Pettit, N. von den Driesch, M. Jansen, A. Pawlis, E. Waks, "Single photon emission from donor bound excitons in ZnSe quantum wells", *Bulletin of the American Physical Society*, G67.00002 (2022).

C.2. **A. Karasahin**, R. M. Pettit, M. M. Jansen, A. Pawlis, and E. Waks, "Quantum emission from Cl doped ZnSe quantum wells", *in Frontiers in Optics/ Laser Science, OSA Technical Digest (Optical Society of America)* (2020).

C.3. **A. Karasahin**, M. Jansen, A. Pawlis, E. Waks, "Donor-bound excitons in Cl doped ZnSe quantum wells", *Bulletin of the American Physical Society*, 65, 1 (2020).

Bibliography

[1] Ashley Montanaro. Quantum algorithms: An overview. *npj Quantum Information*, 2(1):1–8, jan 2016.

[2] Peter W. Shor and John Preskill. Simple proof of security of the BB84 quantum key distribution protocol. *Physical Review Letters*, 85(2):441–444, jul 2000.

[3] Lior Cohen, Elisha S. Matekole, Yoni Sher, Daniel Istrati, Hagai S. Eisenberg, and Jonathan P. Dowling. Thresholded Quantum LIDAR: Exploiting Photon-Number-Resolving Detection. *Physical Review Letters*, 123(20):203601, nov 2019.

[4] Christoph Kloeffel and Daniel Loss. Prospects for spin-based quantum computing in quantum dots. *Annual Review of Condensed Matter Physics*, 4(1):51–81, mar 2013.

[5] John Clarke and Frank K. Wilhelm. Superconducting quantum bits. *Nature*, 453(7198):1031–1042, jun 2008.

[6] Pieter Kok, W. J. Munro, Kae Nemoto, T. C. Ralph, Jonathan P. Dowling, and G. J. Milburn. Linear optical quantum computing with photonic qubits. *Reviews of Modern Physics*, 79(1):135–174, jan 2007.

[7] David P. Divincenzo. The Physical Implementation of Quantum Computation. *Scalable Quantum Computers*, pages 1–13, jan 2005.

[8] Marlan O. Scully and M. Suhail Zubairy. Quantum Optics. *Quantum Optics*, sep 1997.

[9] T. D. Ladd, K. Sanaka, Y. Yamamoto, A. Pawlis, and K. Lischka. Fluorine-doped ZnSe for applications basic solid state physics in quantum information processing. *Physica Status Solidi (B) Basic Research*, 247(6):1543–1546, jun 2010.

[10] Shun Kanai, F. Joseph Heremans, Hosung Seo, Gary Wolfowicz, Christopher P. Anderson, Sean E. Sullivan, Giulia Galli, David D. Awschalom, and Hideo Ohno. Generalized scaling of spin qubit coherence in over 12,000 host materials. feb 2021.

[11] A. Greilich, A. Pawlis, F. Liu, O. A. Yugov, D. R. Yakovlev, K. Lischka, Y. Yamamoto, and M. Bayer. Spin dephasing of fluorine-bound electrons in ZnSe. *Physical Review B - Condensed Matter and Materials Physics*, 85(12), mar 2012.

[12] Johannes Borregaard, Anders Søndberg Sørensen, and Peter Lodahl. Quantum Networks with Deterministic Spin–Photon Interfaces. *Advanced Quantum Technologies*, 2(5-6):1800091, jun 2019.

[13] Ali W. Elshaari, Wolfram Pernice, Kartik Srinivasan, Oliver Benson, and Val Zwiller. Hybrid integrated quantum photonic circuits. *Nature Photonics*, 14(5):285–298, apr 2020.

[14] Gary Wolfowicz, F. Joseph Heremans, Christopher P. Anderson, Shun Kanai, Hosung Seo, Adam Gali, Giulia Galli, and David D. Awschalom. Quantum guidelines for solid-state spin defects. *Nature Reviews Materials*, 6(10):906–925, apr 2021.

[15] David D. Awschalom, Ronald Hanson, Jörg Wrachtrup, and Brian B. Zhou. Quantum technologies with optically interfaced solid-state spins. *Nature Photonics*, 12(9):516–527, aug 2018.

[16] J. R. Weber, W. F. Koehl, J. B. Varley, A. Janotti, B. B. Buckley, C. G. Van De Walle, and D. D. Awschalom. Quantum computing with defects. *Proceedings of the National Academy of Sciences of the United States of America*, 107(19):8513–8518, may 2010.

[17] Matthew E. Trusheim, Benjamin Pingault, Noel H. Wan, Mustafa Gündoğan, Lorenzo De Santis, Romain Debroux, Dorian Gangloff, Carola Purser, Kevin C. Chen, Michael Walsh, Joshua J. Rose, Jonas N. Becker, Benjamin Lienhard, Eric Bersin, Ioannis Paradeisanos, Gang Wang, Dominika Lyzwa, Alejandro R.P. Montblanch, Girish Malladi, Hassaram Bakhru, Andrea C. Ferrari, Ian A. Walmsley, Mete Atatüre, and Dirk Englund. Transform-Limited Photons from a Coherent Tin-Vacancy Spin in Diamond. *Physical Review Letters*, 124(2):023602, jan 2020.

[18] Carlo Bradac, Weibo Gao, Jacopo Forneris, Matthew E. Trusheim, and Igor Aharonovich. Quantum nanophotonics with group IV defects in diamond. *Nature Communications*, 10(1):1–13, dec 2019.

[19] Kaoru Sanaka, Alexander Pawlis, Thaddeus D. Ladd, Klaus Lischka, and Yoshihisa Yamamoto. Indistinguishable photons from independent semiconductor nanostructures. *Physical Review Letters*, 103(5), aug 2009.

[20] Kaoru Sanaka, Alexander Pawlis, Thaddeus D. Ladd, Darin J. Sleiter, Klaus Lischka, and Yoshihisa Yamamoto. Entangling single photons from independently tuned semiconductor nanoemitters. *Nano Letters*, 12(9):4611–4616, sep 2012.

[21] Xiayu Linpeng, Maria L.K. Viitaniemi, Aswin Vishnuradhan, Y. Kozuka, Cameron Johnson, M. Kawasaki, and Kai Mei C. Fu. Coherence Properties of Shallow Donor Qubits in Zn O. *Physical Review Applied*, 10(6):064061, dec 2018.

[22] S. Strauf, P. Michler, M. Klude, D. Hommel, G. Bacher, and A. Forchel. Quantum optical studies on individual acceptor bound excitons in a semiconductor. *Physical Review Letters*, 89(17):177403/1–177403/4, 2002.

[23] D. D. Sukachev, A. Sipahigil, C. T. Nguyen, M. K. Bhaskar, R. E. Evans, F. Jelezko, and M. D. Lukin. Silicon-Vacancy Spin Qubit in Diamond: A Quantum Memory Exceeding 10 ms with Single-Shot State Readout. *Physical Review Letters*, 119(22):223602, nov 2017.

[24] Xiayu Linpeng, Todd Karin, Mikhail V. Durnev, Mikhail M. Glazov, Rüdiger Schott, Andreas D. Wieck, Arne Ludwig, and Kai Mei C. Fu. Optical spin control and coherence properties of acceptor bound holes in strained GaAs. *Physical Review B*, 103(11):115412, mar 2021.

[25] Mete Atatüre, Dirk Englund, Nick Vamivakas, Sang Yun Lee, and Joerg Wrachtrup. Material platforms for spin-based photonic quantum technologies. *Nature Reviews Materials*, 3(5):38–51, apr 2018.

[26] Zhouchen Luo, Shuo Sun, Aziz Karasahin, Allan S. Bracker, Samuel G. Carter, Michael K. Yakes, Daniel Gammon, and Edo Waks. A Spin-Photon Interface Using Charge-Tunable Quantum Dots Strongly Coupled to a Cavity. *Nano Letters*, 19(10):7072–7077, oct 2019.

[27] Alisa Javadi, Dapeng Ding, Martin Hayhurst Appel, Sahand Mahmoodian, Matthias Christian Löbl, Immo Söllner, Rüdiger Schott, Camille Papon, Tommaso Pregnolato, Søren Stobbe, Leonardo Midolo, Tim Schröder, Andreas Dirk Wieck, Arne Ludwig, Richard John Warburton, and Peter Lodahl. Spin-photon interface and spin-controlled photon switching in a nanobeam waveguide. *Nature Nanotechnology*, 13(5):398–403, mar 2018.

[28] K. De Greve, S. M. Clark, D. Sleiter, K. Sanaka, T. D. Ladd, M. Panfilova, A. Pawlis, K. Lischka, and Y. Yamamoto. Photon antibunching and magnetospectroscopy of a single fluorine donor in ZnSe. *Applied Physics Letters*, 97(24):241913, dec 2010.

[29] Alexander Pawlis, Gregor Mussler, Christoph Krause, Benjamin Bennemann, Uwe Breuer, and Detlev Grutzmacher. MBE Growth and Optical Properties of Isotopically Purified ZnSe Heterostructures. *ACS Applied Electronic Materials*, 1(1):44–50, jan 2019.

[30] Erik Kirstein, Evgeny A. Zhukov, Dmitry S. Smirnov, Vitalie Nedelea, Phillip Greve, Ina V. Kalitukha, Viktor F. Sapega, Alexander Pawlis, Dmitri R. Yakovlev, Manfred Bayer, and Alex Greilich. Extended spin coherence of the zinc-vacancy centers in ZnSe with fast optical access. *Communications Materials*, 2(1):1–8, sep 2021.

[31] Darin J. Sleiter, Kaoru Sanaka, Y. M. Kim, Klaus Lischka, Alexander Pawlis, and Yoshihisa Yamamoto. Optical pumping of a single electron spin bound to a fluorine donor in a ZnSe nanostructure. *Nano Letters*, 13(1):116–120, jan 2013.

[32] K. Ohkawa, T. Mitsuyu, and O. Yamazaki. Characteristics of Cl-doped ZnSe layers grown by molecular-beam epitaxy. *Journal of Applied Physics*, 62(8):3216–3221, aug 1987.

[33] H. Morkoç, S. Strite, G. B. Gao, M. E. Lin, B. Sverdlov, and M. Burns. Large-band-gap SiC, III-V nitride, and II-VI ZnSe-based semiconductor device technologies. *Journal of Applied Physics*, 76(3):1363–1398, aug 1994.

[34] S. Pöykkö, M. Puska, and R. Nieminen. Chlorine-impurity-related defects in ZnSe. *Physical Review B - Condensed Matter and Materials Physics*, 57(19):12164–12168, may 1998.

[35] N. V. Bondar', V. V. Tishchenko, and M. S. Brodin. Exciton energy states and photoluminescence spectra of the strained-layer ZnS-ZnSe superlattices. *Semiconductors*, 34(5):568–574, 2000.

[36] Torsten Rieger, Thomas Riedl, Elmar Neumann, Detlev Grützmacher, Jörg K.N. Lindner, and Alexander Pawlis. Strain Compensation in Single ZnSe/CdSe Quantum Wells: Analytical Model and Experimental Evidence. *ACS Applied Materials and Interfaces*, 9(9):8371–8377, mar 2017.

[37] Alexander Pawlis, Gregor Mussler, Christoph Krause, Benjamin Bennemann, Uwe Breuer, and Detlev Grutzmacher. MBE Growth and Optical Properties of Isotopically Purified ZnSe Heterostructures. *ACS Applied Electronic Materials*, 1(1):44–50, jan 2019.

[38] Johanna Janßen, Felix Hartz, Till Huckemann, Christian Kamphausen, Malte Neul, Lars R. Schreiber, and Alexander Pawlis. Low-Temperature Ohmic Contacts to n-ZnSe for all-Electrical Quantum Devices. *ACS Applied Electronic Materials*, 2(4):898–905, apr 2020.

[39] M. C. Tamargo. Structural characterization of GaAs/ZnSe interfaces. *Journal of Vacuum Science & Technology B: Microelectronics and Nanometer Structures*, 6(2):784, jun 1988.

[40] H. Mariette, F. Dalbo, N. Magnea, G. Lentz, and H. Tuffigo. Optical investigation of confinement and strain effects in CdTe/Cd1-xZnxTe single quantum wells. *Physical Review B*, 38(17):12443–12448, dec 1988.

[41] A. V. Kavokin, V. P. Kochereshko, G. R. Posina, I. N. Uraltsev, D. R. Yakovlev, G. Landwehr, R. N. Bicknell-Tassius, and A. Waag. Effect of the electron Coulomb potential on hole confinement in II-VI quantum wells. *Physical Review B*, 46(15):9788–9791, oct 1992.

[42] A. Pawlis, T. Berstermann, C. Brüggemann, M. Bombeck, D. Dunker, D. R. Yakovlev, N. A. Gippius, K. Lischka, and M. Bayer. Exciton states in shallow ZnSe/(Zn,Mg)Se quantum wells: Interaction of confined and continuum electron and hole states. *Physical Review B - Condensed Matter and Materials Physics*, 83(11):115302, mar 2011.

[43] P. J. Dean, D. C. Herbert, C. J. Werkhoven, B. J. Fitzpatrick, and R. N. Bhargava. Donor bound-exciton excited states in zinc selenide. *Physical Review B*, 23(10):4888–4901, may 1981.

[44] G. Bastard. Hydrogenic impurity states in a quantum well: A simple model. *Physical Review B*, 24(8):4714–4722, oct 1981.

[45] O. Homburg, K. Sebald, P. Michler, J. Gutowski, H. Wenisch, and D. Hommel. Negatively charged trion in ZnSe single quantum wells with very low electron densities. *Physical Review B - Condensed Matter and Materials Physics*, 62(11):7413–7419, sep 2000.

[46] Conrad Spindler, Thomas Galvani, Ludger Wirtz, Germain Rey, and Susanne Siebentritt. Excitation-intensity dependence of shallow and deep-level photoluminescence transitions in semiconductors. *Journal of Applied Physics*, 126(17):175703, nov 2019.

[47] Francisco A.P. Osario, Marcos H. Degani, and Oscar Hipalito. Bound impurity in GaAs-Ga1-Al As quantum-well wires. *Physical Review B*, 37(3):1402–1405, jan 1988.

[48] R. T. Senger and K. K. Bajaj. Binding energies of excitons in II-VI compound-semiconductor based quantum well structures. *Physica Status Solidi (B) Basic Research*, 241(8):1896–1900, jul 2004.

[49] Ravitej Uppu, Leonardo Midolo, Xiaoyan Zhou, Jacques Carolan, and Peter Lodahl. Quantum-dot-based deterministic photon–emitter interfaces for scalable photonic quantum technology. *Nature Nanotechnology*, 16(12):1308–1317, oct 2021.

[50] L. J. Rogers, K. D. Jahnke, T. Teraji, L. Marseglia, C. Müller, B. Naydenov, H. Schauffert, C. Kranz, J. Isoya, L. P. McGuinness, and F. Jelezko. Multiple intrinsically identical single-photon emitters in the solid state. *Nature Communications*, 5:4739, jan 2014.

[51] A. Sipahigil, R. E. Evans, D. D. Sukachev, M. J. Burek, J. Borregaard, M. K. Bhaskar, C. T. Nguyen, J. L. Pacheco, H. A. Atikian, C. Meuwly, R. M. Camacho, F. Jelezko, E. Bielejec, H. Park, M. Lončar, and M. D. Lukin. An integrated diamond nanophotonics platform for quantum-optical networks. *Science*, 354(6314):847–850, nov 2016.

[52] R. E. Evans, M. K. Bhaskar, D. D. Sukachev, C. T. Nguyen, A. Sipahigil, M. J. Burek, B. Machielse, G. H. Zhang, A. S. Zibrov, E. Bielejec, H. Park, M. Lončar, and M. D. Lukin. Photon-mediated interactions between quantum emitters in a diamond nanocavity. *Science*, 362(6415):662–665, nov 2018.

[53] Liang Zhai, Matthias C. Löbl, Jan Philipp Jahn, Yongheng Huo, Philipp Treutlein, Oliver G. Schmidt, Armando Rastelli, and Richard J. Warburton. Large-range frequency tuning of a narrow-linewidth quantum emitter. *Applied Physics Letters*, 117(8):083106, aug 2020.

[54] J. Puls, G. V. Mikhailov, S. Schwertfeger, D. R. Yakovlev, F. Henneberger, and W. Faschinger. High-excitation effects in the optical properties of δ-doped ZnSe quantum wells. *Physica Status Solidi (B) Basic Research*, 227(2):331–337, 2001.

[55] M. Hayne, A. Usher, A. S. Plaut, and K. Ploog. Optically induced density depletion of the two-dimensional electron system in GaAs/AlxGa1-xAs heterojunctions. *Physical Review B*, 50(23):17208–17216, dec 1994.

[56] E. A. Zhukov, A. Greilich, D. R. Yakovlev, K. V. Kavokin, I. A. Yugova, O. A. Yugov, D. Suter, G. Karczewski, T. Wojtowicz, J. Kossut, V. V. Petrov, Yu K. Dolgikh, A. Pawlis, and M. Bayer. All-optical NMR in semiconductors provided by resonant cooling of nuclear spins interacting with electrons in the resonant spin amplification regime. *Physical Review B - Condensed Matter and Materials Physics*, 90(8):085311, aug 2014.

[57] Je Hyung Kim, Christopher J.K. Richardson, Richard P. Leavitt, and Edo Waks. Two-Photon Interference from the Far-Field Emission of Chip-Integrated Cavity-Coupled Emitters. *Nano Letters*, 16(11):7061–7066, nov 2016.

[58] Yi hong Wu, Kenta Arai, and Takafumi Yao. Temperature dependence of the photoluminescence of ZnSe/ZnS quantum-dot structures. *Physical Review B - Condensed Matter and Materials Physics*, 53(16):R10485–R10488, apr 1996.

[59] L. Malikova, Wojciech Krystek, Fred H. Pollak, N. Dai, A. Cavus, and M. Tamargo. Temperature dependence of the direct gaps of ZnSe and ZnCdSe. *Physical Review B - Condensed Matter and Materials Physics*, 54(3):1819–1824, jul 1996.

[60] M. Bayer, G. Ortner, O. Stern, A. Kuther, A. A. Gorbunov, A. Forchel, P. Hawrylak, S. Fafard, K. Hinzer, T. L. Reinecke, S. N. Walck, J. P. Reithmaier, F. Klopf, and F. Schäfer. Fine structure of neutral and charged excitons in self-assembled In(Ga)As/(Al) GaAs quantum dots. *Physical Review B - Condensed Matter and Materials Physics*, 65(19):1953151–19531523, may 2002.

[61] P. J. Dean, W. Stutius, G. F. Neumark, B. J. Fitzpatrick, and R. N. Bhargava. Ionization energy of the shallow nitrogen acceptor in zinc selenide. *Physical Review B*, 27(4):2419–2428, feb 1983.

[62] Youngmin Martin Kim. Fluorine Donor Bound Electron Spins As Qubits. *PhD Dissertation Thesis*, pages 1–104, 2013.

[63] M. Oestreich, S. Hallstein, and A. Heberle. Temperature and density dependence of the electron Landé g factor in semiconductors. *Physical Review B - Condensed Matter and Materials Physics*, 53(12):7911–7916, mar 1996.

[64] Yoshihisa Yamamoto, Charles Santori, and Matthew Pelton. Regulated and entangled photons from a single quantum dot. *Physical Review Letters*, 84(11):2513–2516, mar 2000.

[65] Jin Liu, Rongbin Su, Yuming Wei, Beimeng Yao, Saimon Filipe Covre da Silva, Ying Yu, Jake Iles-Smith, Kartik Srinivasan, Armando Rastelli, Juntao Li, and Xuehua Wang. A solid-state source of strongly entangled photon pairs with high brightness and indistinguishability. *Nature Nanotechnology*, 14(6):586–593, apr 2019.

[66] Hui Wang, Hai Hu, T. H. Chung, Jian Qin, Xiaoxia Yang, J. P. Li, R. Z. Liu, H. S. Zhong, Y. M. He, Xing Ding, Y. H. Deng, Qing Dai, Y. H. Huo, Sven Höfling, Chao Yang Lu, and Jian Wei Pan. On-Demand Semiconductor Source of Entangled Photons Which Simultaneously Has High Fidelity, Efficiency, and Indistinguishability. *Physical Review Letters*, 122(11):113602, mar 2019.

[67] Harishankar Jayakumar, Ana Predojević, Thomas Kauten, Tobias Huber, Glenn S. Solomon, and Gregor Weihs. Time-bin entangled photons from a quantum dot. *Nature Communications*, 5(1):1–5, jun 2014.

[68] Maximilian Prilmüller, Tobias Huber, Markus Müller, Peter Michler, Gregor Weihs, and Ana Predojević. Hyperentanglement of Photons Emitted by a Quantum Dot. *Physical Review Letters*, 121(11):110503, sep 2018.

[69] Christoph Simon, Hugues De Riedmatten, Mikael Afzelius, Nicolas Sangouard, Hugo Zbinden, and Nicolas Gisin. Quantum repeaters with photon pair sources and multimode memories. *Physical Review Letters*, 98(19):190503, may 2007.

[70] Francesco Basso Basset, Mauro Valeri, Emanuele Roccia, Valerio Muredda, Davide Poderini, Julia Neuwirth, Nicolò Spagnolo, Michele B. Rota, Gonzalo Carvacho, Fabio Sciarrino, and Rinaldo Trotta. Quantum key distribution with entangled photons generated on demand by a quantum dot. *Science Advances*, 7(12):6379, mar 2021.

[71] Sergei Slussarenko and Geoff J. Pryde. Photonic quantum information processing: A concise review. *Applied Physics Reviews*, 6(4):041303, oct 2019.

[72] Vittorio Giovannetti, Seth Lloyd, and Lorenzo MacCone. Advances in quantum metrology. *Nature Photonics*, 5(4):222–229, mar 2011.

[73] Daniel Huber, Marcus Reindl, Johannes Aberl, Armando Rastelli, and Rinaldo Trotta. Semiconductor quantum dots as an ideal source of polarization-entangled photon pairs on-demand: A review. *Journal of Optics (United Kingdom)*, 20(7):073002, jun 2018.

[74] Yu Ming He, Oliver Iff, Nils Lundt, Vasilij Baumann, Marcelo Davanco, Kartik Srinivasan, Sven Höfling, and Christian Schneider. Cascaded emission of single photons from the biexciton in monolayered WSe 2. *Nature Communications*, 7(1):1–6, nov 2016.

[75] S. Marcet, R. André, and S. Francoeur. Excitons bound to Te isoelectronic dyads in ZnSe. *Physical Review B - Condensed Matter and Materials Physics*, 82(23):235309, dec 2010.

[76] F. Sarti, G. Muñoz Matutano, D. Bauer, N. Dotti, S. Bietti, G. Isella, A. Vinattieri, S. Sanguinetti, and M. Gurioli. Multiexciton complex from extrinsic centers in AlGaAs epilayers on Ge and Si substrates. *Journal of Applied Physics*, 114(22):224314, dec 2013.

[77] Nicola Dotti, Francesco Sarti, Sergio Bietti, Alexander Azarov, Andrej Kuznetsov, Francesco Biccari, Anna Vinattieri, Stefano Sanguinetti, Marco Abbarchi, and Massimo Gurioli. Germanium-based quantum emitters towards a time-reordering entanglement scheme with degenerate exciton and biexciton states. *Physical Review B - Condensed Matter and Materials Physics*, 91(20):205316, may 2015.

[78] S. M. Ulrich, S. Strauf, P. Michler, G. Bacher, and A. Forchel. Triggered polarization-correlated photon pairs from a single CdSe quantum dot. *Applied Physics Letters*, 83(9):1848–1850, aug 2003.

[79] E. Moreau, I. Robert, L. Manin, V. Thierry-Mieg, J. M. Gérard, and I. Abram. Quantum cascade of photons in semiconductor quantum dots. *Physical Review Letters*, 87(18):183601–1–183601–4, oct 2001.

[80] V. D. Kulakovskii, G. Bacher, R. Weigand, T. Kümmell, A. Forchel, E. Borovitskaya, K. Leonardi, and D. Hommel. Fine structure of biexciton emission in symmetric and asymmetric CdSe/ZnSe single quantum dots. *Physical Review Letters*, 82(8):1780–1783, feb 1999.

[81] I. A. Akimov, A. Hundt, T. Flissikowski, and F. Henneberger. Fine structure of the trion triplet state in a single self-assembled semiconductor quantum dot. *Applied Physics Letters*, 81(25):4730–4732, dec 2003.

[82] X. Y. Chang, X. M. Dou, B. Q. Sun, Y. H. Xiong, Z. C. Niu, H. Q. Ni, and D. S. Jiang. Optical transitions of positively charged excitons and biexcitons in single InAs quantum dots. *Journal of Applied Physics*, 106(10):103716, nov 2009.

[83] A. J. Bennett, M. A. Pooley, R. M. Stevenson, M. B. Ward, R. B. Patel, A. Boyer De La Giroday, N. Sköd, I. Farrer, C. A. Nicoll, D. A. Ritchie, and A. J. Shields. Electric-field-induced coherent coupling of the exciton states in a single quantum dot. *Nature Physics*, 6(12):947–950, oct 2010.

[84] R. M. Stevenson, R. J. Young, P. See, D. G. Gevaux, K. Cooper, P. Atkinson, I. Farrer, D. A. Ritchie, and A. J. Shields. Magnetic-field-induced reduction of the exciton polarization splitting in InAs quantum dots. *Physical Review B - Condensed Matter and Materials Physics*, 73(3):033306, jan 2006.

[85] Stefan Seidl, Martin Kroner, Alexander Högele, Khaled Karrai, Richard J. Warburton, Antonio Badolato, and Pierre M. Petroff. Effect of uniaxial stress on excitons in a self-assembled quantum dot. *Applied Physics Letters*, 88(20):203113, may 2006.

[86] John D. Joannopoulos, Steven G. Johnson, Joshua N. Winn, and Robert D. Meade. Photonic crystals: Molding the flow of light. *Photonic Crystals: Molding the Flow of Light (Second Edition)*, page 446, 2011.

[87] Juntao Li, Thomas P. White, Liam O'Faolain, Alvaro Gomez-Iglesias, and Thomas F. Krauss. Systematic design of flat band slow light in photonic crystal waveguides. *Optics Express*, 16(9):6227, apr 2008.

[88] Dirk Englund, Ilya Fushman, and Jelena Vučković. General recipe for designing photonic crystal cavities. *Optics Express*, 13(16):5961, aug 2005.

[89] V. S.C. Manga Rao and S. Hughes. Single quantum-dot Purcell factor and β factor in a photonic crystal waveguide. *Physical Review B - Condensed Matter and Materials Physics*, 75(20):205437, may 2007.

[90] Sylvain Combrié, Nguyen Vi Quynh Tran, and Alfredo De Rossi. Directive emission from high-Q photonic crystal cavities through band folding. *Optics InfoBase Conference Papers*, 79(4):041101, jan 2009.

[91] Edo Waks and Jelena Vuckovic. Dipole induced transparency in drop-filter cavity-waveguide systems. *Physical Review Letters*, 96(15):153601, 2006.

[92] Shuo Sun, Hyochul Kim, Glenn S. Solomon, and Edo Waks. A quantum phase switch between a single solid-state spin and a photon. *Nature Nanotechnology*, 11(6):539–544, feb 2016.

[93] A. R.A. Chalcraft, S. Lam, D. O'Brien, T. F. Krauss, M. Sahin, D. Szymanski, D. Sanvitto, R. Oulton, M. S. Skolnick, A. M. Fox, D. M. Whittaker, H. Y. Liu, and M. Hopkinson. Mode structure of the L3 photonic crystal cavity. *Applied Physics Letters*, 90(24):241117, jun 2007.